IOP Publishing New J. Phys. 26 (2024) 073009 https://doi.org/10.1088/1367-2630/ad5b14

New Journal of Physics
The open access journal at the forefront of physics

Deutsche Physikalische Gesellschaft DPG
IOP Institute of Physics

Published in partnership with: Deutsche Physikalische Gesellschaft and the Institute of Physics

OPEN ACCESS

RECEIVED
27 March 2024

REVISED
8 June 2024

ACCEPTED FOR PUBLICATION
23 June 2024

PUBLISHED
4 July 2024

PAPER

Topological boundary modes in nonlinear dynamics with chiral symmetry

Di Zhou

Key Lab of Advanced Optoelectronic Quantum Architecture and Measurement (MOE) and School of Physics, Beijing Institute of Technology, Beijing 100081, People's Republic of China
Department of Physics, University of Illinois, Urbana-Champaign, 61801, United States of America

E-mail: dizhou@bit.edu.cn

Keywords: topological physics, nonlinear dynamics, non-spatial symmetry

Abstract

Particle-hole symmetry and chiral symmetry play a pivotal role in multiple areas of physics, yet they remain unstudied in systems with nonlinear interactions whose nonlinear normal modes do not exhibit $\mathbf{U}(1)$-gauge symmetry. In this work, we establish particle-hole symmetry and chiral symmetry in such systems. Chiral symmetry ensures the quantization of the Berry phase of nonlinear normal modes and categorizes the topological phases of nonlinear dynamics. We show topologically protected static boundary modes in chiral-symmetric nonlinear systems. Furthermore, we demonstrate amplitude-induced nonlinear topological phase transition in chiral-symmetric nonlinear dynamics. Our theoretical framework extends particle-hole and chiral symmetries to nonlinear dynamics, whose nonlinear modes do not necessarily yield $\mathbf{U}(1)$-gauge symmetry.

1. Introduction

Non-spatial symmetries govern the fundamental principles of physics in multiple areas. In high-energy physics, the combination of particle-hole, parity, and time-reversal symmetries dictate the existence of anti-particles [1]. In quantum mechanics, time-reversal symmetry demands that eigenstates with half-integer spins must be doubly degenerate, which is known as the Kramers' degeneracy [2, 3]. In soft matter and engineering physics, chiral symmetry reveals the chiral image of elastic floppy modes and states of self-stress [4–7], governing the elastic failure and stability [8–11], respectively. Additionally, in condensed-matter physics, time-reversal, particle-hole, and chiral symmetries classify topological phases of matter in a 'ten-fold' way [12–15]. This classification enables fundamental understanding of symmetry-protected topological phases with potential applications for quantum information technology [14, 16–20].

Non-spatial symmetries have been the subject of extensive study in both linear [21–24] and nonlinear systems [25–37]. For instance, time-reversal and parity symmetries have been thoroughly explored in the context of elastic, electrical and photonic structures [38–45], enabling novel designs of microcavities [46], circuit metamaterials [47], and plasmonic waveguides [48]. Other non-spatial symmetries, such as particle-hole symmetry and chiral symmetry, have been studied in linear systems and special nonlinear systems, such as the Kerr and beyond-Kerr nonlinear interactions [49–52] that preserve $\mathbf{U}(1)$-gauge symmetry on the nonlinear wave functions [53, 54], and Rock-paper-Scissors cycles in zero-sum games [55–59]. However, the rigorous definition and establishment of (anti-unitary) particle-hole symmetry and (unitary) chiral symmetry have not been addressed in nonlinear systems that do not exhibit $\mathbf{U}(1)$-gauge symmetry in their nonlinear wave functions.

Nonlinear interactions are ubiquitous in nature, such as nonlinear elastic [38, 60–63] and electrical structures [64, 65], circadian rhythms of living cells [66], and quantum fluids in optical lattices [67]. These nonlinear mechanisms possess unique features that cannot be observed in linear systems, including soliton propagation [68, 69], nonlinear localized modes [70], bifurcation [71], and chaos [72]. Given the significant

influence of particle-hole symmetry and chiral symmetry on linear systems, it is intriguing to ask what happens when these two symmetries encounter nonlinear dynamics.

In this work, we study the nonlinear dynamics using generalized nonlinear Schrödinger equations. We extend the concept of particle-hole symmetry and chiral symmetry to nonlinear dynamics, where the nonlinear modes do not necessarily possess $\mathbf{U}(1)$-gauge symmetry. We investigate the nontrivial consequences on nonlinear topological physics that are derived from particle-hole and chiral symmetries. Our motivation derives from the history of linear topological insulators, where although extensive research had been conducted in topological physics, there continued to be fundamental importance in the 'non-spatial' classification of symmetry-protected topological phases [12, 13]. Such a 'ten-fold' non-spatial-symmetry classification significantly enhances the potential application of topological physics, such as topological quantum computation.

To explore the impact of particle-hole and chiral symmetries on nonlinear topological physics, we investigate the geometric phase of nonlinear normal modes under the adiabatic evolution of system parameters. We find that, interestingly, this adiabatic geometric phase can be quantized by chiral symmetry, and defines the topologically trivial and non-trivial phases of the generalized nonlinear Schrödinger equations. In the topologically non-trivial phase, nonlinear modes appear at the open boundaries of the system. These modes possess 'topological protection' as they show resistance against disturbances to both the modes themselves and the nonlinear interactions. Furthermore, due to chiral symmetry, the frequencies of nonlinear boundary modes are pinned at zero. Consequently, these topologically robust modes are static in time. We use a Lotka–Volterra model [73–75] to demonstrate the practical application of our results. The Lotka–Volterra model, originally designed for biological cycles, has also demonstrated relevance in understanding boson condensation within driven-dissipative systems [55, 76, 77]. Finally, we demonstrate the amplitude-induced topological phase transition that is unique to nonlinear dynamics.

The organization of this paper is as follows. Section 2 defines the model, which is the generalized nonlinear Schrödinger equations. Section 3 derives the adiabatic geometric phase in nonlinear normal modes. This adiabatic phase is separated into two parts: the Berry phase of nonlinear normal modes, and the component that is unique to nonlinear systems. In section 4, we discuss two types of non-spatial symmetries: particle-hole symmetry and chiral symmetry. Notably, we demonstrate the quantization of the Berry phase of nonlinear normal modes under chiral symmetry. Section 5 investigates the topological phases in both linear and nonlinear regimes and discusses the nonlinear topological boundary modes. In section 6, we extend our theoretical framework to a more general model, demonstrating an amplitude-induced nonlinear topological phase transition within chiral-symmetric nonlinear systems. Section 7 raises several proposals of the experimental realization for our theoretical framework.

2. The model

Nonlinear dynamics, including electrical structures [64], and nonlinear materials [78, 79], can be described by generalized nonlinear Schrödinger equations. Unlike Bose–Einstein condensates and Kerr-nonlinear optics, nonlinear interactions in these classical structures do not possess $\mathbf{U}(1)$-gauge symmetry in their nonlinear normal modes [40, 70]. To establish particle-hole symmetry and chiral symmetry in generalized nonlinear Schrödinger equations, we consider a two-dimensional square lattice with the primitive vectors $\hat{e}_x$ and $\hat{e}_y$, as illustrated in figure 1. The unit cells are identified by two integers n_x and n_y, corresponding to their positions $\boldsymbol{r} = n_x\hat{e}_x + n_y\hat{e}_y$. Within each unit cell, there exist two classical fields, namely $\Psi_{\boldsymbol{r}}^{(1)}$ and $\Psi_{\boldsymbol{r}}^{(2)}$. The dynamics of these classical variables are governed by the following generalized nonlinear Schrödinger equations,

$$\begin{aligned} \mathrm{i}\partial_t \Psi_{\boldsymbol{r}}^{(1)} &= +\sum_{\langle \boldsymbol{r}',\boldsymbol{r}\rangle, i'=1,2} U\left(\Psi_{\boldsymbol{r}}^{(1)}, \Psi_{\boldsymbol{r}'}^{(i')}\right), \\ \mathrm{i}\partial_t \Psi_{\boldsymbol{r}}^{(2)} &= -\sum_{\langle \boldsymbol{r}',\boldsymbol{r}\rangle, i'=1,2} U\left(\Psi_{\boldsymbol{r}}^{(2)}, \Psi_{\boldsymbol{r}'}^{(i')}\right). \end{aligned} \tag{1}$$

Here, $\langle \boldsymbol{r}',\boldsymbol{r}\rangle$ denotes the nearest-neighbor sites $\boldsymbol{r}$ and $\boldsymbol{r}'$ in the square lattice. $U(\Psi_{\boldsymbol{r}}^{(i)}, \Psi_{\boldsymbol{r}'}^{(i')})$ is a real-coefficient quadratic polynomial that describes the nonlinear interaction between the classical fields $\Psi_{\boldsymbol{r}}^{(i)}$ and $\Psi_{\boldsymbol{r}'}^{(i')}$:

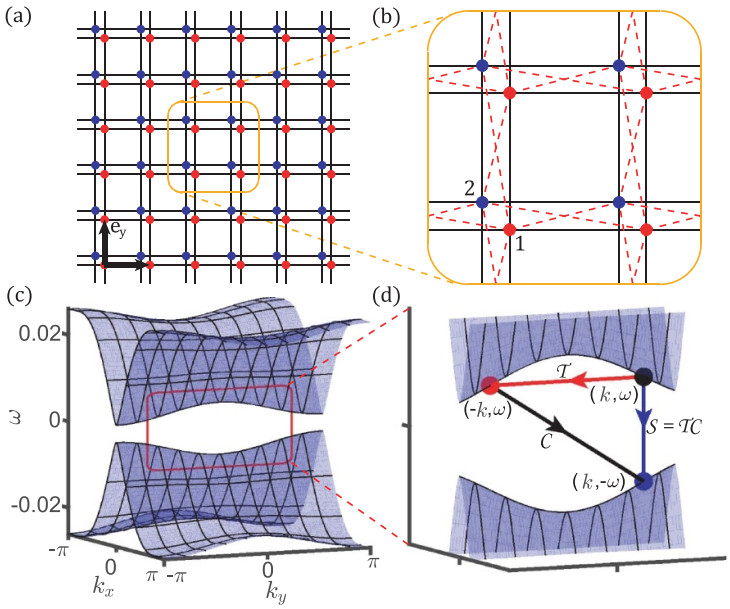

Figure 1. The model of nonlinear dynamics. (a) The diatomic two-dimensional square lattice, with the primitive vectors $\hat{e}_x$ and $\hat{e}_y$ represented by the black arrows. (b) Red and blue dots mark the 1 and 2 sites within the unit cell. The nonlinear interactions within 1 or 2 sites (between 1 and 2 sites) are denoted by black solid lines (red dashed lines). We use the quadratic nonlinearity as the example for our nonlinear topological physics. (c) The nonlinear band structure [80, 81] of the model with the quadratic interactions specified in equation (2), where $\epsilon = 0.001$. $g_x = 0.9$, $g_y = 0.1$, and mode amplitudes $A = 10\epsilon$. (d) Enlarged nonlinear band structure in (c) illustrates the relationships among time-reversal, particle-hole, and chiral partner modes.

$$U\left(\Psi_{\boldsymbol{r}}^{(i)}, \Psi_{\boldsymbol{r}'}^{(i')}\right) = \left(\epsilon + \Psi_{\boldsymbol{r}}^{(i)}\right)\Psi_{\boldsymbol{r}'}^{(i')}\left[\left(n_x - n_x'\right)\left(1 - \delta_{ii'}\right) + \left(-\delta_{n_x,n_x'}\delta_{n_y,n_y'} + \sum_{j=x,y} g_j|n_j - n_j'|\right)\delta_{ii'}\right], \tag{2}$$

where ϵ represents the linear on-site potential, and g_j for $j = x, y$ accounts for the nonlinear effects between the nearest-neighbor classical fields. These constant parameters are positive and real numbers, with $\epsilon \ll 1$ utilized to emphasize the significance of nonlinear effects. This nonlinear interaction is pictorially represented by the black solid and red dashed lines in figure 1(b).

This model is capable of describing a number of physical systems. When the amplitude of the classical fields is much smaller than ϵ, this classical model is in the linear regime. The topological boundary modes in this linearized classical model can mimic the quantum fermionic edge states within the Bogoliubov–de Gennes Hamiltonian of topological superconductors [82, 83]. When the mode amplitude becomes comparable or greater than ϵ, the model is highly nonlinear in the classical field variables. In this regime, the *static solutions* of this nonlinear Schrödinger-type dynamics can mimic the *static solutions* of the Lotka–Volterra model [73, 84, 85], which we elaborate later in section 5.

This nonlinear interaction, as represented by equation (2), yields the inequality:

$$U\left(\mathrm{e}^{\mathrm{i}\theta}\Psi_{\boldsymbol{r}}^{(i)}, \mathrm{e}^{\mathrm{i}\theta}\Psi_{\boldsymbol{r}'}^{(i')}\right) \neq \mathrm{e}^{\mathrm{i}\theta}U\left(\Psi_{\boldsymbol{r}}^{(i)}, \Psi_{\boldsymbol{r}'}^{(i')}\right), \tag{3}$$

indicating that the $\mathbf{U}(1)$-gauge symmetry in the nonlinear wave functions is broken. To further clarify this statement, we denote the nonlinear wave function as the following form

$$\Psi = \left(\ldots, \Psi_{\boldsymbol{r}}^{(1)}, \Psi_{\boldsymbol{r}}^{(2)}, \ldots\right)^{\top}. \tag{4}$$

This is a column vector with $2N$ components, where N is the number of diatomic unit cells, and $\to p$ denotes matrix transpose. In a concise representation, equation (1) can be written as

$$\mathrm{i}\partial_t\Psi = H(\Psi) \tag{5}$$

where $H(\Psi)$ is a nonlinear mapping of Ψ, and is called the nonlinear Hamiltonian. It is a $2N\times 1$ column vector with each element given by equation (2). Again, we emphasize that the nonlinear Hamiltonian does not preserve the $\mathbf{U}(1)$-gauge symmetry in the nonlinear modes by showing

$$H\left(\mathrm{e}^{\mathrm{i}\theta}\Psi\right)\neq \mathrm{e}^{\mathrm{i}\theta}H(\Psi)\,. \tag{6}$$

In section 4, we will demonstrate that the nonlinear model in equation (1) respects particle-hole symmetry and chiral symmetry.

3. Adiabatic geometric phase of nonlinear normal modes

In this section, we derive the geometric phase that arises from the adiabatic evolution of nonlinear normal modes in the model presented in equation (1). The adiabatic geometric phase is especially useful in characterizing the topological phases and predicting the existence of topological boundary modes in nonlinear dynamics.

When the amplitudes of classical fields are much smaller than ϵ, the nonlinear Hamiltonian can be linearized into a two-band matrix Hamiltonian $\hat{H}_{\boldsymbol{k}}$ [83]. This Hamiltonian describes the oscillation of classical variables governed by the eigenfrequency $\omega=\omega(\boldsymbol{k})$, where the wavevector $\boldsymbol{k}=(k_x,k_y)$ resides in the two-dimensional Brillouin zone.

Nonlinearities become increasingly important as mode amplitude rises, making nonlinear normal modes significantly deviate from sinusoidal waves of linear systems [64, 70, 86, 87]. Specifically, nonlinear normal modes with the plane-wave format satisfy the expression

$$\Psi_{\boldsymbol{k}}=\left(\Psi_{\boldsymbol{k}}^{(1)}\left(\boldsymbol{k}\cdot\boldsymbol{r}-\omega t\right),\Psi_{\boldsymbol{k}}^{(2)}\left(\boldsymbol{k}\cdot\boldsymbol{r}-\omega t+\phi_{\boldsymbol{k}}\right)\right)^{\top} \tag{7}$$

according to the nonlinear extension of the Bloch theorem [70, 88]. Here, $\Psi_{\boldsymbol{k}}^{(1)}(\theta)$ and $\Psi_{\boldsymbol{k}}^{(2)}(\theta)$ represent the 2π-periodic non-sinusoidal functions, while $\phi_{\boldsymbol{k}}$ characterizes the relative phase between these wave components. The frequencies of these nonlinear normal modes, denoted by $\omega=\omega(\boldsymbol{k},A)$, are influenced by both the wavevectors $\boldsymbol{k}$ and mode amplitudes A, deviating from their linear counterparts. It is worth emphasizing that in nonlinear systems, the number of nonlinear modes can exceed the degrees of freedom, allowing nonlinear localized modes [70, 89] and 'looped band structures' [51, 90–92] to emerge from the effect of bifurcation. However, in this work, our scope is limited to the simple case that bifurcation does not occur, and these additional excitations do not emerge from the nonlinear dynamics. Thus, plane-wave nonlinear normal modes can be uniquely defined based on their amplitude, wavevector, and frequency, allowing the nonlinear system to be effectively described as a 'two-band nonlinear model.'

We adiabatically evolve the plane-wave nonlinear normal mode as the wavevector $\boldsymbol{k}=\boldsymbol{k}(t)$ follows a closed trajectory C in the Brillouin zone [3]. Based on the nonlinear extension of the adiabatic theorem [93, 94], at time t, the nonlinear normal mode follows the ansatz

$$\Psi=\Psi_{\boldsymbol{k}(t)}\left(-\int_0^t\omega\left(t',\boldsymbol{k}(t')\right)\mathrm{d}t'-\gamma(t)\right), \tag{8}$$

where $\gamma(t)$ denotes the phase shift of the nonlinear normal mode during the adiabatic evolution. When the wavevector $\boldsymbol{k}$ completes a closed-loop travel in the Brillouin zone, the wave function acquires a phase γ_C, known as the adiabatic geometric phase [95, 96].

As per the Whitham modulation theory [97–99], during the adiabatic evolution of the wavevector $\boldsymbol{k}$ in reciprocal space, the mode amplitude A and relative phase $\phi_{\boldsymbol{k}}$ (as defined in equation (7)) should change slowly. Consequently, the adiabatic phase, denoted by γ_C, can be separated into two components: $\gamma_C=\gamma_C^{(\mathrm{B})}+\gamma_C^{(\mathrm{NL})}$. The first term, $\gamma_C^{(\mathrm{B})}$, is referred to as the Berry phase of nonlinear normal modes, which originates from the change in the relative phase $\phi_{\boldsymbol{k}}$. On the other hand, the second term, $\gamma_C^{(\mathrm{NL})}$, arises from the change in the mode amplitude. In the upcoming discussion, we will examine $\gamma_C^{(\mathrm{B})}$ and $\gamma_C^{(\mathrm{NL})}$ individually.

As described in appendix A, the derivation of the Berry phase of nonlinear normal modes involves computing the evolution of the relative phase $\phi_{\boldsymbol{k}}$ as the wavevector $\boldsymbol{k}$ undergoes adiabatic changes:

$$\gamma_C^{(\mathrm{B})}=\oint_C\frac{\sum\limits_l\left(l|\psi_{l\boldsymbol{k}}^{(2)}|^2\nabla_{\boldsymbol{k}}\phi_{\boldsymbol{k}}-\mathrm{i}\sum\limits_{i=1,2}\psi_{l\boldsymbol{k}}^{(i)*}\nabla_{\boldsymbol{k}}\psi_{l\boldsymbol{k}}^{(i)}\right)}{\sum\limits_{l'}l'\left(|\psi_{l'\boldsymbol{k}}^{(1)}|^2+|\psi_{l'\boldsymbol{k}}^{(2)}|^2\right)}\cdot\mathrm{d}\boldsymbol{k}. \tag{9}$$

Here, $\psi_{l\boldsymbol{k}}^{(i)} = (2\pi)^{-1}\int_0^{2\pi} \mathrm{e}^{-\mathrm{i}l\theta}\Psi_{\boldsymbol{k}}^{(i)}\mathrm{d}\theta$ is the lth Fourier component of the nonlinear wave, $\Psi_{\boldsymbol{k}}^{(i)}$, with $i = 1, 2$. We emphasize that for Schrödinger equations with linear [3] or nonlinear interactions that exhibit $\mathbf{U}(1)$-gauge symmetry [91] in their eigenstates, the eigenmodes can be described using fundamental harmonics only. This reduces equation (9) to the Berry phase in [95], $\gamma_{C,\mathrm{linear}}^{(\mathrm{B})} = \mathrm{i}\oint_C \mathrm{d}\boldsymbol{k}\cdot\langle\Psi_{\boldsymbol{k}}|\nabla_{\boldsymbol{k}}|\Psi_{\boldsymbol{k}}\rangle$ (see appendix A for details). Usually, $\gamma_C^{(\mathrm{B})}$ is *not quantized* in systems without symmetry constraints. However, $\gamma_C^{(\mathrm{B})}$ can be quantized if non-spatial symmetries are incorporated in the system, which we address in section 4.3.

The Whitham modulation theory [97–99] also indicates that mode amplitude should change during adiabatic evolution. This effect gives rise to an additional contribution to the adiabatic geometric phase [95], denoted as $\gamma_C^{(\mathrm{NL})}$. However, as we will demonstrate in section 4.3, chiral symmetry imposes a constraint that causes the amplitudes of the two wave components of a nonlinear normal mode to be equal. This constraint results in the mode amplitude staying unchanged, up to the normalization factor of the wave function. Consequently, we have found that the adiabatic geometric phase $\gamma_C^{(\mathrm{NL})}$ vanishes under such constraints. This vanishing result is derived in [95] and in appendix A. As a result, the Berry phase of nonlinear normal modes, $\gamma_C^{(\mathrm{B})}$, is the only contribution to the adiabatic geometric phase. Under the constraint of chiral symmetry, this Berry phase takes quantized values and classifies the topological phases of the nonlinear dynamics.

4. Particle-hole symmetry, chiral symmetry, and topological index of nonlinear systems

In this section, we establish particle-hole symmetry and chiral symmetry for nonlinear dynamics. We show that chiral symmetry can be used to quantize the Berry phase of nonlinear normal modes in the model described by equation (1). This quantized index serves as a topological invariant and defines the topologically trivial and non-trivial phases of the nonlinear dynamics.

We briefly review time-reversal symmetry that has been well-established in nonlinear dynamics [49, 70, 100, 101]. The nonlinear system is time-reversal invariant if the equations of motion remain unchanged under the time-reversal transformation $(\Psi_{\boldsymbol{r}}^{(1)}(t), \Psi_{\boldsymbol{r}}^{(2)}(t)) \to (\Psi_{\boldsymbol{r}}^{(1)*}(-t), \Psi_{\boldsymbol{r}}^{(2)*}(-t))$. This invariance arises from the real-coefficient polynomials of the nonlinear interactions in terms of the field variables. The formal expression of time-reversal symmetry is $\mathcal{T}H(\Psi) - H(\mathcal{T}\Psi) = 0$, where $H(\Psi)$ is the nonlinear Hamiltonian, and the time-reversal operator, $\mathcal{T} = \mathcal{K}; t \to -t$, involving complex conjugation and reversing the sign of time. Here, $H(\mathcal{T}\Psi)$ means that we perform the time-reversal operation on the nonlinear wave Ψ, and then we operate on $\mathcal{T}\Psi$ using the nonlinear Hamiltonian (nonlinear mapping) H. This symmetry implies that for a nonlinear wave $\Psi_{\boldsymbol{k}}$ in a time-reversal symmetric model, there exists a time-reversed partner solution with the wavevector $-\boldsymbol{k}$, denoted as $\Psi_{-\boldsymbol{k}} = \mathcal{T}\Psi_{\boldsymbol{k}} = (\Psi_{\boldsymbol{k}}^{(1)*}(\boldsymbol{k}\cdot\boldsymbol{r} + \omega t), \Psi_{\boldsymbol{k}}^{(2)*}(\boldsymbol{k}\cdot\boldsymbol{r} + \omega t + \phi_{\boldsymbol{k}}))^{\top}$, as pictorially indicated by the red arrow and dot in figure 1(d).

The time-reversal operator satisfies $\mathcal{T}^2 = 1$ and is anti-unitary, aligning with the operator for linear Schrödinger equation of spinless particles [2, 102]. In the linear regime, time-reversal symmetry simplifies to the conventional form, $\mathcal{T}\hat{H}_{\boldsymbol{k}}\mathcal{T}^{-1} = \hat{H}_{-\boldsymbol{k}}$, where $\hat{H}_{\boldsymbol{k}}$ represents the linearized Hamiltonian in reciprocal space.

4.1. Particle-hole symmetry of nonlinear dynamics

Here, we introduce the particle-hole operator and its corresponding symmetry for nonlinear systems.

In a particle-hole symmetric system, the motion equations in equation (1) remain unchanged under the particle-hole transformation, $(\Psi_{\boldsymbol{r}}^{(1)}, \Psi_{\boldsymbol{r}}^{(2)}) \to (\Psi_{\boldsymbol{r}}^{(2)*}, \Psi_{\boldsymbol{r}}^{(1)*})$. This invariance is equivalently captured by the constraint,

$$\mathcal{C}H(\Psi) + H(\mathcal{C}\Psi) = 0, \qquad \mathcal{C} = \mathrm{I}_N \otimes \sigma_x\mathcal{K}, \tag{10}$$

where $\mathcal{C}$ is the particle-hole operator, I_N is the $N \times N$ identity matrix, and σ_x is the Pauli matrix. One important characteristic of the particle-hole operator we have defined is its *anti-unitary* property, which arises from the complex conjugation involved in the operator. This property, in turn, results in the reversal of the frequency and momentum of the original nonlinear wave (see equation (7)) in the system under particle-hole transformation. Therefore, for a nonlinear normal mode $\Psi_{\boldsymbol{k}}$ with the wavevector $\boldsymbol{k}$ and frequency ω, the particle-hole-symmetric model has a corresponding nonlinear sister solution with a wavevector $-\boldsymbol{k}$ and frequency $-\omega$, denoted as

$$\Psi_{-\boldsymbol{k},-} = \mathcal{C}\Psi_{\boldsymbol{k}} = \left(\Psi_{\boldsymbol{k}}^{(2)*}(\boldsymbol{k}\cdot\boldsymbol{r} - \omega t), \Psi_{\boldsymbol{k}}^{(1)*}(\boldsymbol{k}\cdot\boldsymbol{r} - \omega t - \phi_{\boldsymbol{k}})\right)^{\top}, \tag{11}$$

as depicted by the black arrow in figure 1(d). The particle-hole operator satisfies $\mathcal{C}^2 = 1$ and is anti-unitary, aligning with the operator defined for linear systems [2, 83].

These results, including the particle-hole symmetry presented in equation (10) and the particle-hole-partner mode in equation (11), naturally apply to linear and nonlinear systems that respect the $\mathbf{U}(1)$-gauge symmetry. Furthermore, in these $\mathbf{U}(1)$-symmetric systems, equation (10) can be reduced to the well-studied format defined in reciprocal space, namely $\mathcal{C}\hat{H}_{\boldsymbol{k}}\mathcal{C}^{-1} = -\hat{H}_{-\boldsymbol{k}}$.

4.2. Chiral symmetry of nonlinear dynamics

Chiral symmetry naturally arises in nonlinear systems when both time-reversal and particle-hole symmetries are present. The model described by equation (1) remains unchanged under the chiral transformation $(\Psi_{\boldsymbol{r}}^{(1)}(t), \Psi_{\boldsymbol{r}}^{(2)}(t)) \to (\Psi_{\boldsymbol{r}}^{(2)}(-t), \Psi_{\boldsymbol{r}}^{(1)}(-t))$. Mathematically, chiral symmetry is expressed as the constraint on the nonlinear Hamiltonian given by

$$\mathcal{S}H(\Psi) + H(\mathcal{S}\Psi) = 0, \qquad \mathcal{S} = \mathcal{T}\cdot\mathcal{C}, \tag{12}$$

where $\mathcal{S} = \mathcal{T}\cdot\mathcal{C}$ represents the chiral symmetry operator that combines the effects of time-reversal and particle-hole transformations. It is worth noting that the resulting chiral symmetry operator, which is a combination of time-reversal and particle-hole symmetry operators expressed as $\mathcal{S} = \mathcal{T}\cdot\mathcal{C}$, is *unitary* in nature. This is due to the anti-unitary nature of both time-reversal and particle-hole symmetry operators, which cancels out to produce a unitary chiral symmetry operator that is critical for characterizing the topological properties of the nonlinear system, which we address in the following subsection. Thus, for a nonlinear normal mode $\Psi_{\boldsymbol{k}}$ with frequency ω, chiral symmetry predicts the existence of a partner solution with frequency $-\omega$, denoted as

$$\Psi_{\boldsymbol{k},-} = \mathcal{S}\Psi_{\boldsymbol{k}} = \left(\Psi_{\boldsymbol{k}}^{(2)}(\boldsymbol{k}\cdot\boldsymbol{r}+\omega t), \Psi_{\boldsymbol{k}}^{(1)}(\boldsymbol{k}\cdot\boldsymbol{r}+\omega t-\phi_{\boldsymbol{k}})\right)^{\top}. \tag{13}$$

This relationship is depicted by the green arrow and dot in figure 1(d). This chiral operator is unitary and yields $\mathcal{S}^2 = 1$, agreeing perfectly with the chiral operator for linear topological insulators.

These results, including the chiral symmetry presented in equation (12) and the chiral-partner mode in equation (13), naturally apply for linear and nonlinear systems that respect the $\mathbf{U}(1)$-gauge symmetry. Furthermore, in these $\mathbf{U}(1)$-symmetric systems, equation (12) can be reduced to the well-studied format [102–104] defined in reciprocal space, namely $\mathcal{S}\hat{H}_{\boldsymbol{k}}\mathcal{S}^{-1} = -\hat{H}_{\boldsymbol{k}}$. Finally, our study highlights an important aspect of chiral-symmetric nonlinear systems. We find that the chiral-symmetric partner nonlinear mode swaps the two wave components of a nonlinear normal mode. This swapping leads to a result where the two wave components in a nonlinear normal mode share the same mode amplitude.

Our nonlinear model exhibits time-reversal, particle-hole, and chiral symmetries, which is the extension of symmetry class BDI defined in the ten-fold classification of linear topological insulators [103].

4.3. Berry phase of nonlinear normal modes quantized by chiral symmetry

In a purely linear Schrödinger equation, the summation of Berry phases across all energy bands is always zero due to the topological triviality of the fiber bundle [3] associated with a complete and orthogonal set of eigenbasis in a matrix Hamiltonian [3]. Combined with chiral symmetry, this sum rule naturally results in the quantization of linear Berry phase [105]. However, this conclusion does not hold for nonlinear dynamics, because nonlinear normal modes do not necessarily have completeness and orthogonality when matrix analysis fails. Therefore, the quantization of Berry phase of nonlinear normal modes in a chiral-symmetric nonlinear system, as expressed in equation (9), remains an open question.

Here, we demonstrate that under chiral symmetry, the Berry phase of nonlinear normal modes still remains quantized for nonlinear systems. Moreover, the quantization of the Berry phase of nonlinear normal modes suggests that it can serve as a potential topological index for characterizing the topological phases of the underlying nonlinear dynamics.

To demonstrate that chiral symmetry is still capable of quantizing the Berry phase of nonlinear normal modes, we consider the nonlinear normal mode $\Psi_{\boldsymbol{k},-} = \mathcal{S}\Psi_{\boldsymbol{k}}$, which is the chiral-partner mode of $\Psi_{\boldsymbol{k}}$. We perform an adiabatic evolution on this chiral-partner mode by slowly varying the wavevector $\boldsymbol{k}(t)$ along a closed-loop trajectory C in the Brillouin zone. When we adiabatically evolve the chiral-symmetric partner mode, $\Psi_{\boldsymbol{k},-}$, this mode can be considered as having a frequency of ω but with the arrow of time reversed. Consequently, the mode acquires a term $\gamma(t)$ in its phase variable, via

$$\Psi(t) = \Psi_{\boldsymbol{k}(t),-}\left(\int_0^t \omega(t', \boldsymbol{k}(t'))\,\mathrm{d}t' + \gamma(t)\right). \tag{14}$$

Substituting this result into the nonlinear motion equations, namely $\mathrm{i}\partial_t\Psi_{\boldsymbol{k}(t),-} = H(\Psi_{\boldsymbol{k}(t),-})$, we can compute the geometric phase when the wavevector $\boldsymbol{k}$ travels along the trajectory C. This adiabatic evolution

allows the chiral-symmetric nonlinear mode to obtain the adiabatic geometric phase, $\gamma_C = \gamma_C^{(\mathrm{B})}$ (note that $\gamma_C^{(\mathrm{NL})} = 0$ in chiral-symmetric systems, as shown in appendix A), from which the Berry phase of nonlinear normal modes, $\gamma_C^{(\mathrm{B})}$, is obtained:

$$\gamma_C^{(\mathrm{B})} = \oint_C \frac{\sum_l \left(l|\psi_{l\boldsymbol{k}}^{(1)}|^2 \nabla_{\boldsymbol{k}}\phi_{\boldsymbol{k}} + \mathrm{i}\sum_{i=1,2} \psi_{l\boldsymbol{k}}^{(i)*} \nabla_{\boldsymbol{k}} \psi_{l\boldsymbol{k}}^{(i)} \right)}{\sum_{l'} l' \left(|\psi_{l'\boldsymbol{k}}^{(1)}|^2 + |\psi_{l'\boldsymbol{k}}^{(2)}|^2 \right)} \cdot \mathrm{d}\boldsymbol{k}. \tag{15}$$

Since both equations (9) and (15) describe the same Berry phase of nonlinear normal modes under the same evolution trajectory, we equate them, and obtain the result

$$\gamma_C^{(\mathrm{B})} = \frac{1}{2}\oint_C \nabla_{\boldsymbol{k}}\phi_{\boldsymbol{k}} \cdot \mathrm{d}\boldsymbol{k} = n\pi, \quad n = 0, 1. \tag{16}$$

This equation demonstrates the quantization of the Berry phase of nonlinear normal modes under the constraint of chiral symmetry, which serves as the topological invariant of the considered nonlinear dynamics. $n = 0, 1$ correspond to the nonlinear topologically trivial and non-trivial phases, respectively. Due to the quantized nature of this Berry phase, it cannot change continuously upon the variations of system parameters, including the mode amplitudes and coupling parameters. Below, we leverage the invariance of this topological number to investigate the corresponding nonlinear topological edge modes.

It is noteworthy that the Berry phase of nonlinear normal modes has been shown to take quantized values when spatial reflection symmetry is present [88]. However, the model described by equation (1) lacks this spatial symmetry, rendering spatial symmetries ineffective in quantizing the Berry phase. Instead, chiral symmetry, a non-spatial symmetry, plays a crucial role in quantizing the Berry phase of nonlinear normal modes.

5. Nonlinear topological phases and boundary modes

We have demonstrated the topological invariance of the Berry phase of nonlinear normal modes using chiral symmetry. In this section, we exemplify the impact of this topological number on the nonlinear physics, where the interactions are specified as the example in equation (2) with the quadratic nonlinearities. Specifically, we investigate the topological phases and the corresponding boundary physics of the system in both the linear and nonlinear regimes.

5.1. Topological phases and boundary modes in the linear regime

When the quadratic nonlinearities are small compared to the linear parts, the nonlinear system can be approximated as linear Schrödinger equations. This regime is valid when mode amplitudes $A \ll \epsilon$. This allows us to perform a momentum-space decomposition and simplify the linearized equations of motion using the equation, $\mathrm{i}\partial_t \Psi_{\boldsymbol{k}} = \hat{H}_{\boldsymbol{k},\omega}\Psi_{\boldsymbol{k}}$, where the the linear wave function is represented as $\Psi_{\boldsymbol{k}} = (\Psi_{\boldsymbol{k}}^{(1)}, \Psi_{\boldsymbol{k}}^{(2)})^\top$, the matrix Hamiltonian, $\hat{H}_{\boldsymbol{k},\omega}$, reads

$$\hat{H}_{\boldsymbol{k},\omega} = 2\epsilon\sigma_y \sin k_x + \epsilon\sigma_z \left(-1 + 2\sum_{j=x,y} g_j \cos k_j \right), \tag{17}$$

where $\boldsymbol{k} = (k_x, k_y)$ is the wavevector within the two-dimensional Brillouin zone, and $\sigma_{x,y,z}$ are Pauli matrices. This Hamiltonian possesses chiral symmetry, namely a unitary chiral symmetry operator $\mathcal{S} = \sigma_x$ anti-commutes with it [83, 102]: $\{\sigma_x, \hat{H}_{\boldsymbol{k},\omega}\} = 0$.

The Hamiltonian $\hat{H}_{\boldsymbol{k},\omega}$ has multiple phases. Specifically, when the interaction parameters are in the grey region of figure 2(a) (i.e. the interaction parameters satisfy $|g_y| \geqslant |g_x - 1/2| \bigcup |g_y| \geqslant |g_x + 1/2|$), the system becomes gapless, as the linear band structures touch at a pair of zero-frequency points. As a result, the linear Berry phase becomes singular and ill-defined when the integration trajectory passes through these gapless points. When the linear bands touch at the gapless points, the corresponding static eigenstates are given by

$$\Psi_r(t) = (1, \pm 1)^\top \mathrm{e}^{\mathrm{i}\boldsymbol{k}_w \cdot \boldsymbol{r}}/\sqrt{2}, \tag{18}$$

whose frequency and wavevector are $\omega = 0$ and $\pm\boldsymbol{k}_w$, respectively. For the parameters that lie in the region of $|g_y| \geqslant |g_x - 1/2|$, we have the wavevectors $\boldsymbol{k}_w = (0, \arccos[(1 - 2g_x)/2g_y])$. When the parameters are in the

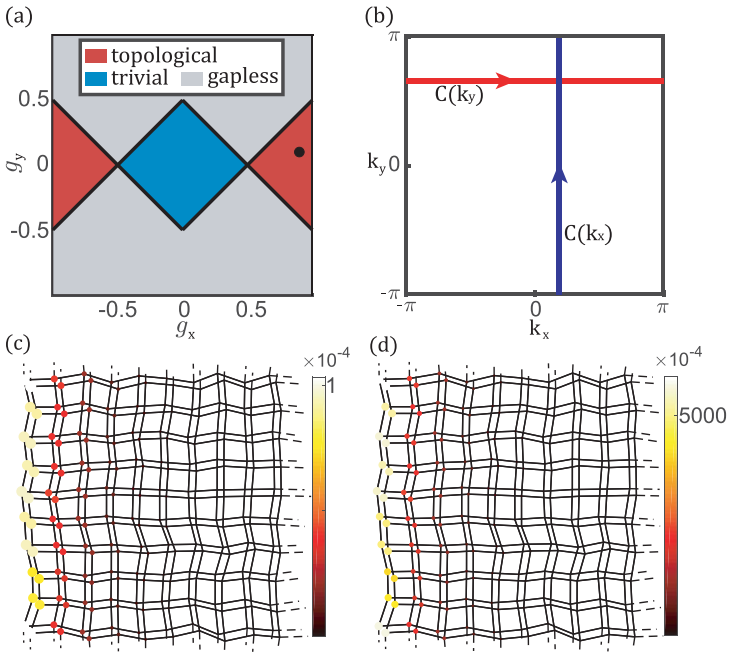

Figure 2. Topological phases and boundary modes. (a) Nonlinear topological phase diagram of the model with quadratic nonlinearities. (b) Brillouin zone with the integration trajectories of Berry phases of nonlinear normal modes indicated. (c) Disks' size and color represent the spatial profile of the weakly nonlinear topological edge mode. (d) Spatial distribution of the topological boundary mode in the highly nonlinear regime.

region $|g_y| \geqslant |g_x + 1/2|$, the wavevectors are given by $\boldsymbol{k}_w = (\pi, \arccos[(1+2g_x)/2g_y])$. We note that the zero-frequency nature of these gapless bulk states stems from the chiral symmetry [106].

On the other hand, in the blue region of figure 2(a) (the parameters yield $|g_y| < |g_x - 1/2| \bigcap |g_y| < |g_y + 1/2|$), and in the red region of figure 2(a) (with the parameters that yield $-g_x + 1/2 < g_y < g_x - 1/2 \bigcup g_x + 1/2 < g_y < -g_x - 1/2$), the lattice is fully gapped and the linear Berry phase becomes well-defined:

$$\lim_{A\to 0} \gamma_C^{(\mathrm{B})}(A) = \mathrm{i} \oint_C \mathrm{d}\boldsymbol{k} \cdot \langle \Psi_{\boldsymbol{k}} | \nabla_{\boldsymbol{k}} | \Psi_{\boldsymbol{k}} \rangle, \tag{19}$$

where C is the closed-loop trajectory for the adiabatic evolution of the wavevector $\boldsymbol{k}$ in the two-dimensional Brillouin zone. Specifically, we define two types of closed-loop integration trajectories, $C(k_y) : k_x = -\pi \to \pi; k_y$ and $C(k_x) : k_y = -\pi \to \pi; k_x$, which integrate over all k_x for a given k_y and all k_y for a given k_x, respectively. These two integration trajectories correspond to the red and blue lines in figure 2(b), respectively. The linear Berry phase corresponding to the horizontal trajectory $C(k_y)$ is denoted as $\gamma_{C(k_y)}$, while that corresponding to the vertical trajectory $C(k_x)$ is denoted as $\gamma_{C(k_x)}$.

Due to the chiral symmetric nature of the linearized Hamiltonian [83], these Berry phases, namely $\gamma_{C(k_y)}$ and $\gamma_{C(k_x)}$, are guaranteed to have integer multiples of π. Moreover, due to the fully gapped nature of the linear band structure, the Berry phases $\gamma_{C(k_y)}$ and $\gamma_{C(k_x)}$ remain unchanged for any k_x and k_y ranging from $-\pi$ to π. To characterize the topological phases of the linearized model, we define the '2D polarization [107]' as a measure of the linear Berry phases averaged by the Brillouin zone,

$$\lim_{A\to 0} \boldsymbol{R}_{\mathrm{T}}(A) = \frac{1}{2\pi^2} \int_{-\pi}^{\pi} \left[\lim_{A\to 0} \gamma_{C(k_y)}^{(\mathrm{B})}(A)\, \mathrm{d}k_y \hat{e}_x + \lim_{A\to 0} \gamma_{C(k_x)}^{(\mathrm{B})}(A)\, \mathrm{d}k_x \hat{e}_y \right]. \tag{20}$$

When the parameters are in the red region of figure 2(a), the topological polarization is given by $\lim_{A\to 0} \boldsymbol{R}_{\mathrm{T}}(A) = \hat{e}_x$, indicating that the linear system is in the topological phase. On the other hand, when the parameters are within the blue region of figure 2(a), the topological polarization becomes $\lim_{A\to 0} \boldsymbol{R}_{\mathrm{T}}(A) = 0$, indicating that the system is in the topologically trivial regime.

According to the principle of bulk-boundary correspondence in topological band theory, the behavior of the system at the boundary is determined by the topological invariant derived from the bulk bands of the lattice. In the red region of figure 2(a), the topological polarization vector takes the value $\lim_{A\to 0} \boldsymbol{R}_{\mathrm{T}}(A) = \hat{e}_x$,

indicating the emergence of topologically protected boundary modes in the system. These boundary modes can be analytically solved using the Jackiw–Rebbi-type solution,

$$\begin{pmatrix} \Psi_{\boldsymbol{r}}^{(1)}(t) \\ \Psi_{\boldsymbol{r}}^{(2)}(t) \end{pmatrix} = A\mathrm{e}^{\mathrm{i}k_y n_y}\left(\mathrm{e}^{-\kappa_+(k_y)n_x} - \mathrm{e}^{-\kappa_-(k_y)n_x}\right)\begin{pmatrix} 1 \\ -1 \end{pmatrix}, \tag{21}$$

where A is the mode amplitude, k_y is the wave number in the transverse y-direction, and the spatial decay rates $\kappa_\pm(k_y)$ yield $\kappa_\pm(k_y) > 0$. This edge mode is exponentially localized on the left open boundary of the square lattice. In contrast, in the topologically trivial phase with the parameters that lie in the blue region of figure 2(a), the topological polarization vector takes the trivial value of $\lim_{A\to 0}\boldsymbol{R}_{\mathrm{T}}(A) = 0$, indicating the absence of topological boundary modes in this linear non-topological phase.

Chiral symmetry of the linearized Hamiltonian leads to an important property in the frequency spectrum of the bulk modes. This ensures that the frequencies of the bulk modes arise in pairs of $\pm\omega$, reflecting the chiral symmetry of the Hamiltonian. This property in the bulk mode frequencies has significant implications for the frequencies of topological edge states in the system. In particular, the frequency of the topological edge state is constrained to be pinned at zero. This is because, if the frequency of the topological state, ω, is nonzero, then a partner topological state with the frequency of $-\omega$ must also arise at the same boundary. These two boundary states can couple and open a band gap on the lattice boundary, violating the topological protection of the edge states. Therefore, topological edge states must have zero frequency and do not evolve in time, satisfying the static condition $\partial_t \Psi_{\boldsymbol{r}}^{(i)} = 0$ for $i = 1, 2$ and for all $\boldsymbol{r}$. The static nature of topological boundary modes remains valid for the nonlinear system as chiral symmetry extends to the fully nonlinear regime.

5.2. Topological phases and boundary modes in the nonlinear regime

We now consider the topological phases and the corresponding boundary modes in the Schrödinger-type equations in the nonlinear regime.

Intriguingly, even in the strongly nonlinear regime, the system remains gapless when the parameters are in the grey-shaded regime of figure 2(a). This is because nonlinear zero-frequency bulk modes can still arise in the nonlinear regime of the system, maintaining the system's gapless nature. The nonlinear static bulk modes can be analytically obtained by imposing the condition $\partial_t \Psi_{\boldsymbol{r}}^{(i)} = 0$ for $i = 1, 2$ and for all $\boldsymbol{r}$, because chiral symmetry assures the frequency of the nonlinear gapless mode to stay at zero. The nonlinear mode in the lattice system is described by equation (18), which is identical to that obtained from the linearized model. The presence of zero-frequency nonlinear bulk modes in the parameter region defined by the grey regime of figure 2(a) yields the closure of the nonlinear band gap, which we define as the 'nonlinear gapless phase' of the system.

The system with parameters in the blue and red regimes of figure 2(a) is in the nonlinear fully gapped phase, because these phases are devoid of the previously discussed zero-frequency nonlinear bulk modes. This property allows the topological numbers of the system to be well-defined and invariant as mode amplitudes rise. Thus, we define the 2D topological polarization of the lattice in the fully nonlinear regime:

$$\boldsymbol{R}_{\mathrm{T}}(A) = \frac{1}{2\pi^2}\int_{-\pi}^{\pi}\left[\gamma^{(\mathrm{B})}_{C(k_y)}(A)\,\mathrm{d}k_y\hat{e}_x + \gamma^{(\mathrm{B})}_{C(k_x)}(A)\,\mathrm{d}k_x\hat{e}_y\right], \tag{22}$$

where the integration trajectories, namely $C(k_y)$ and $C(k_x)$, are the same as those defined in the linear topological regime and is pictorially depicted in figure 2(b). The red-shaded parameter regime shown in figure 2(a) corresponds to the nonlinear topological phase of the system described by the nonlinear Schrödinger equation in equation (1). In this regime, the topological polarization takes the form $\boldsymbol{R}_{\mathrm{T}}(A) = \hat{e}_x$, indicating the presence of nonlinear topological boundary modes at the edges of the lattice. We can calculate the spatial profile of these boundary modes by imposing static boundary conditions and solving for the corresponding eigenstates. The resulting static nonlinear mode is described by equation (21) and is exponentially localized on the left open boundary of the lattice. In the blue-shaded regime of figure 2(a), the system is in the nonlinear topologically trivial phase as described by the nonlinear Schrödinger equation in equation (1). The topological polarization in this regime takes the form $\boldsymbol{R}_{\mathrm{T}}(A) = 0$, indicating that there are no nonlinear topological boundary modes present at the edges of the lattice.

A remarkable feature of the system under consideration is its topological invariance under increasing mode amplitudes in both the non-trivial and trivial phases. This phenomenon arises from the fact that mode amplitudes have a global effect on the nonlinear dynamics of the system and do not alter the topological properties of the lattice. This explains the invariance of the topological Berry phases and polarization for growing mode amplitudes.

5.3. Applications to the static modes in other nonlinear models

To further explore the implications of the previous results for nonlinear systems, we investigate the static nonlinear modes in a different nonlinear model, namely the Lotka–Volterra network. Lotka–Volterra model is especially useful in describing the boson condensation in driven-dissipative setups [55, 76, 77]. To this end, we study the following nonlinear equations of motion with Lotka–Volterra-type nonlinear interactions,

$$\begin{aligned}\partial_t \Psi_{\boldsymbol{r}}^{(1)} &= \sum_{\boldsymbol{r}',i'=1,2} U\left(\Psi_{\boldsymbol{r}}^{(1)}, (-1)^{i'+1}\Psi_{\boldsymbol{r}'}^{(i')}\right),\\ \partial_t \Psi_{\boldsymbol{r}}^{(2)} &= \sum_{\boldsymbol{r}',i'=1,2} U\left(-\Psi_{\boldsymbol{r}}^{(2)}, (-1)^{i'+1}\Psi_{\boldsymbol{r}'}^{(i')}\right).\end{aligned} \tag{23}$$

Although the *dynamical* properties between the Lotka–Volterra model and the Schrödinger-type nonlinear equations in equation (1) are significantly different [108], their *static* properties are remarkably similar, thanks to the presence of chiral symmetry. The reason is as follows.

In the Schrödinger equation, chiral symmetry ensures that the frequencies of nonlinear normal modes emerge in pairs of $\pm\omega$. Therefore, nonlinear topological mode must have zero-frequency, because if the frequency of the topological mode were non-zero, a chiral-partner topological mode with the frequency of $-\omega$ must appear. These two topological modes can interfere and break their topological nature. As a result, the nonlinear topological mode must be static. This static nonlinear topological mode is equivalent to setting $\mathrm{i}\partial_t \Psi_{\boldsymbol{r}}^{(i)} = 0$ in the Schrödinger equation. On the other hand, the stationary solutions in the Lotka–Volterra model are obtained by setting $\partial_t \Psi_{\boldsymbol{r}}^{(i)} = 0$. This finding suggests that the (Schrödinger) static mode is very much similar as the (Lotka–Volterra) static mode, because these two zero-frequency solutions are obtained by substituting $\mathrm{i}\partial_t \Psi_{\boldsymbol{r}}^{(i)} = 0$ and $\partial_t \Psi_{\boldsymbol{r}}^{(i)} = 0$ in the Schrödinger and Lotka–Volterra models, respectively.

The notion of drawing a comparison between the static solution of the Lotka–Volterra and Schrödinger models originates from seminal works [4–11, 109–112], which established an analogy between the static properties of the elastic compatibility matrix and the static solutions in chiral-symmetric Schrödinger equations. The topological properties of the elastic compatibility matrix are defined by introducing an auxiliary chiral-symmetric Schrödinger equation, where we can compute the topological index of this auxiliary Schrödinger equation. We then utilize this topological number of the auxiliary Schrödinger to describe the topology of the static elastic modes in the elastic compatibility matrix, although the dynamical features of these two systems differ significantly.

Building upon this notion, the static solutions for both the Schrödinger and Lotka–Volterra models can be obtained by setting $\partial_t \Psi_{\boldsymbol{r}}^{(i)} = 0$ for $i = 1, 2$ and all $\boldsymbol{r}$. This analogy facilitates the derivation of the static nonlinear boundary mode in equation (23). The phase diagram of the Lotka–Volterra-type model is depicted by figure 2(a), comprising three distinct regions: the nonlinear gapless, topologically non-trivial, and trivial phases, represented by the grey, red, and blue-shaded areas, respectively.

The Lotka–Volterra-type model exhibits topologically distinct boundary properties in the red and blue areas of the phase diagram. In the red parameter region, the model exhibits the emergence of nonlinear static edge modes from the boundary of the square lattice. These edge modes are in line with the derived nonlinear topological polarization of $\boldsymbol{R}_{\mathrm{T}}(A) = \hat{e}_x$. It should be noted that the population of species must be real and positive numbers, which imposes a constraint on our analysis. Under this constraint, we obtain the nonlinear boundary mode

$$\begin{pmatrix} \Psi_{\boldsymbol{r}}^{(1)}(t) \\ \Psi_{\boldsymbol{r}}^{(2)}(t) \end{pmatrix} = A\left(\mathrm{e}^{-\kappa_+(k_y=0)n_x} - \mathrm{e}^{-\kappa_-(k_y=0)n_x}\right)\begin{pmatrix} 1 \\ 1 \end{pmatrix}, \tag{24}$$

where A is the mode amplitude. The spatial decay rate satisfies $\kappa_\pm(k_y = 0) > 0$, and is explicitly expressed in appendix B. This result indicates that the nonlinear boundary mode is exponentially localized on the left open boundary of the system, confirming its topological nature. The spatial decay rate of the nonlinear boundary mode is in perfect agreement with the decay properties of the topological edge modes in the linear and nonlinear regimes of the Schrödinger-type equations in equation (1). Moreover, the nonlinear boundary mode corresponds to the nonlinear topological polarization, $\boldsymbol{R}_{\mathrm{T}}(A) = \hat{e}_x$, in the topologically non-trivial phase. In contrast to the red region, the blue region of the phase diagram of the Lotka–Volterra-type model is devoid of nonlinear topological static modes. This behavior is in line with the derived trivial nonlinear topological polarization, $\boldsymbol{R}_{\mathrm{T}}(A) = 0$.

To validate the analytical results of the emergence of nonlinear topological boundary modes in the Lotka–Volterra-type model, we perform numerical simulations and present the results in figures 2(c), (d) and 3. The numerical simulations confirm the emergence of the nonlinear topological modes on the open

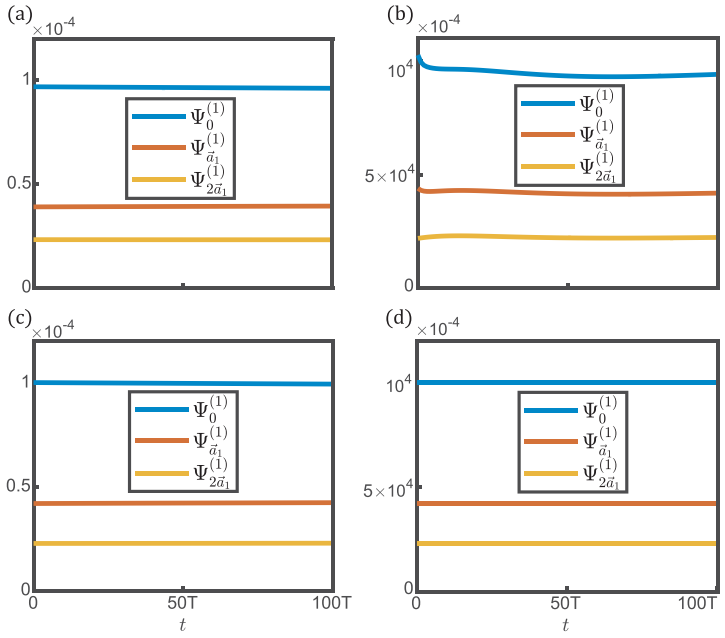

Figure 3. The temporal evolutions of topologically protected boundary modes are shown in (a) and (b) for the weakly nonlinear and fully nonlinear regimes, respectively. In both cases, the modes evolve for $t = 100T$ and still maintain their stability. The temporal profiles for the weakly nonlinear and fully nonlinear modes without introducing disturbances on the wave functions are shown in (c) and (d), respectively.

boundary that cuts the topological polarization vector $\boldsymbol{R}_{\mathrm{T}}(A) = \hat{e}_x$, as predicted by the analytical results. This topologically protected mode exhibits high stability in both temporal and spatial aspects, highlighting its robustness against small perturbations or fluctuations. We initialize the mode with $\pm 10\%$ spatial fluctuations and $\pm 10\%$ spatial variations in the nonlinear interactions, as shown by the bond lengths in figures 2(c) and (d). The numerical simulations indicate that the nonlinear topological mode remains highly stable even after $t = 10^2 T$ of self-oscillation, both in the weakly and strongly nonlinear regimes. The characteristic period of the nonlinear normal mode in the fully nonlinear regime is $T = 2\pi$. The stability of the nonlinear topological mode confirms its robustness and reliability against small perturbations or fluctuations. To further verify the temporal stability of the nonlinear topological mode, we initialize the nonlinear mode in a regular square lattice *without* the random fluctuations in the spatial profile of the nonlinear topological mode and *without* the fluctuations in the nonlinear interactions. As shown in figures 3(c) and (d), in both weakly and fully nonlinear regimes, the mode remains free from oscillatory behavior and exhibits temporal stability.

Chiral symmetry has notable effects on these nonlinear topological boundary modes. Firstly, this symmetry locks the frequencies of topological modes at zero, regardless of their amplitudes. These static modes are distinct from spatial symmetry-induced topological modes, which are sensitive to amplitudes and prone to losing nonlinear stability [38, 80]. Secondly, chiral symmetric nonlinear topological modes are unaffected by the breakdown of spatial symmetries, as observed in figures 2(c) and (d). Conversely, spatial symmetry-induced topological modes are quickly disrupted by spatial symmetry-breaking boundary conditions.

6. Nonlinear topological index and boundary modes for more general models

Having previously established particle-hole symmetry and chiral symmetry in a diatomic square lattice, we now explore whether the same nonlinear topological index and boundary modes persist in more general nonlinear models. To address this, we turn our attention to a different lattice structure, namely the honeycomb lattice, where each unit cell contains four sites. In our analysis, we delve into the implications of chiral symmetry, the quantized Berry phase of nonlinear normal modes, and the existence of nonlinear topological boundary modes. Notably, we investigate two distinct boundary conditions: one with a *zigzag open boundary* (as depicted in figure 4), and the other with an *armchair open boundary* (illustrated in figure 5).

The model under consideration is a four-site unit cell honeycomb lattice, where each site is labeled by position vectors $\boldsymbol{r}_A(\boldsymbol{n})$, $\boldsymbol{r}_B(\boldsymbol{n})$, $\boldsymbol{r}_C(\boldsymbol{n})$, and $\boldsymbol{r}_D(\boldsymbol{n})$. Here, $\boldsymbol{n} = (n_1, n_2)$ denotes the unit cell indices in the honeycomb lattice, with n_1 and n_2 representing the lattice indices. The position of the considered unit cell is

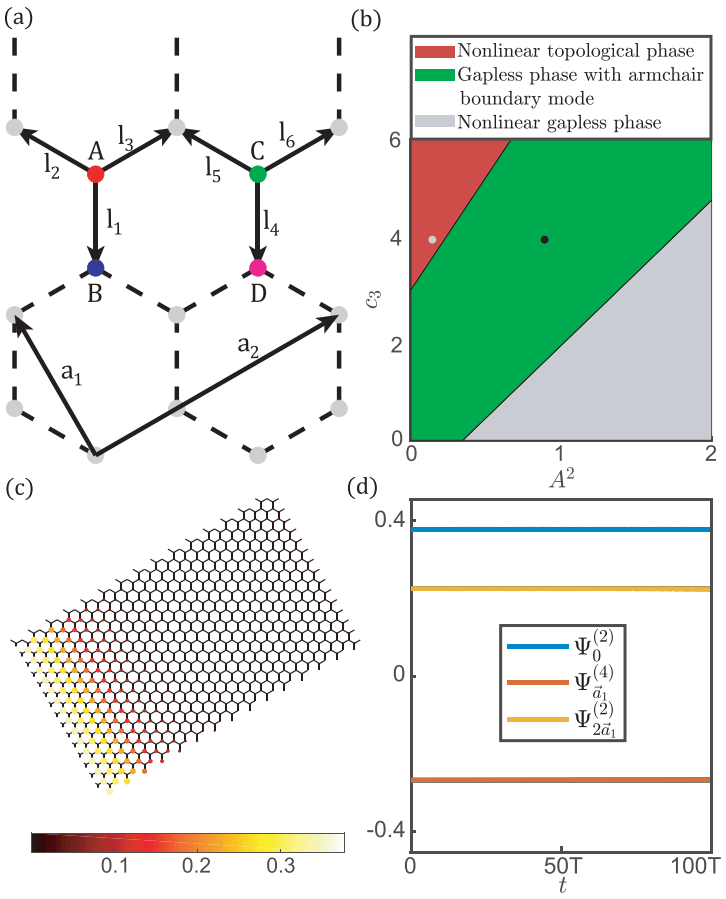

Figure 4. The nonlinear topological honeycomb lattice exhibits chiral symmetry. The lattice is subject to a zigzag open boundary condition along the lattice direction of $\boldsymbol{a}_2$, while a periodic boundary condition is chosen for $\boldsymbol{a}_1$. (a) In the lattice's unit cell, there are four sites labeled as A, B, C, and D. These sites are connected by nonlinear interacting bonds denoted as $\boldsymbol{l}_i$ for $i = 1, 2, 3, 4, 5, 6$. The primitive vectors, represented by black arrows $\boldsymbol{a}_1$ and $\boldsymbol{a}_2$, define the lattice structure. (b) The nonlinear topological phase diagram illustrates the different phases within the honeycomb lattice. (c) We observe a mode profile of the nonlinear topological boundary mode localized on the left bottom boundary of the lattice. (d) This mode remains stable over time, as shown in the temporal profile.

given by $\boldsymbol{r}(\boldsymbol{n}) = n_1\boldsymbol{a}_1 + n_2\boldsymbol{a}_2$, where $\boldsymbol{a}_1 = \ell(3\sqrt{3}/2, 3/2)$ and $\boldsymbol{a}_2 = \ell(-\sqrt{3}/2, 3/2)$ are the primitive vectors for the honeycomb lattice. $\boldsymbol{r}_X(\boldsymbol{n}) = \boldsymbol{r}_X + n_1\boldsymbol{a}_1 + n_2\boldsymbol{a}_2$ marks the position for the site $X = A, B, C, D$. Within this lattice, nonlinear bonds connect neighboring sites, denoted as $\boldsymbol{l}_1$, $\boldsymbol{l}_2$, $\boldsymbol{l}_3$, $\boldsymbol{l}_4$, $\boldsymbol{l}_5$, and $\boldsymbol{l}_6$ (as shown in figure 4). The wave functions for the sites are represented by $\Psi_{\boldsymbol{r}}^{(i)}$, where $i = 1, 2, 3, 4$ corresponds to sites A, B, C, and D. The nonlinear equations of motion for these sites take the form:

$$\mathrm{i}\partial_t \Psi_{\boldsymbol{r}}^{(j)} = \sum_{\langle \boldsymbol{r}, \boldsymbol{r}' \rangle} f_i\left(\Psi_{\boldsymbol{r}}^{(j)}, \Psi_{\boldsymbol{r}'}^{(j')}\right) \tag{25}$$

where $j = 1, 2, 3, 4$ denotes the sites within a unit cell, corresponding to the four sites A, B, C, and D. $\langle \boldsymbol{r}, \boldsymbol{r}' \rangle$ represents nearest-neighbor connections. The nonlinear interaction function is given by:

$$f_i(x, y) = c_i y + d_i \left[(\mathrm{Re}\, y)^3 + \mathrm{i}\,(\mathrm{Im}\, y)^3\right]. \tag{26}$$

This minimal model is a suitable candidate that breaks the $\mathbf{U}(1)$-gauge symmetry and exhibits nonlinear topological phase transitions. The parameters c_i and d_i (for $i = 1, 2, 3, 4, 5, 6$) are real and constant. This specific nonlinear interaction is adopted in [88] and can be realized in active topoelectrical circuits [86]. To maintain chiral symmetry, we impose the condition:

$$f_{i+3}(x, y) = -f_i(x, y), \qquad \text{for} \quad i = 1, 2, 3. \tag{27}$$

Under this constraint, the nonlinear Hamiltonian exhibits chiral symmetry. Specifically, the nonlinear equations of motion can be expressed in the form of a nonlinear Schrödinger equation: $\mathrm{i}\partial_t \Psi_{\boldsymbol{r}} = H(\Psi_{\boldsymbol{r}})$,

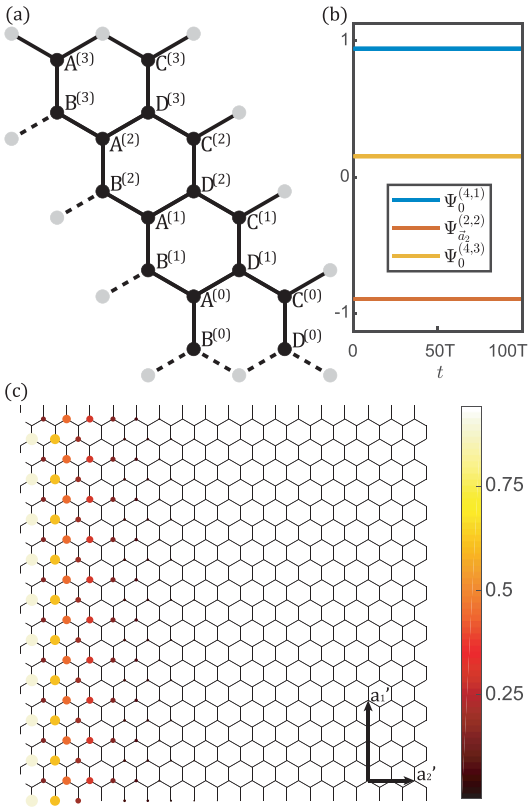

Figure 5. Nonlinear boundary modes in the honeycomb lattice. The lattice is subjected to an armchair open boundary condition in the lattice direction of $\boldsymbol{a}_2'$ and a periodic boundary condition in the lattice direction of $\boldsymbol{a}_1'$. (a) The unit cell is enlarged to a 16-site unit cell, ensuring compatibility with the armchair boundary condition. (b) The temporal profile of the nonlinear boundary mode. (c) The spatial profile of the nonlinear boundary mode under the armchair boundary condition.

where $\Psi_{\boldsymbol{r}} = (\Psi_{\boldsymbol{r}}^{(1)}, \Psi_{\boldsymbol{r}}^{(2)}, \Psi_{\boldsymbol{r}}^{(3)}, \Psi_{\boldsymbol{r}}^{(4)})^{\top}$. This nonlinear Hamiltonian yields the chiral symmetry relationship as expressed in equation (12), where the chiral operator now reads $\mathcal{S} = \sigma_x \otimes I_2$. This symmetry property leads to the quantization of the Berry phase of nonlinear normal modes and the emergence of sister nonlinear normal modes, as mathematically demonstrated in appendix D. Notably, under the *zigzag open boundary condition*, a nonlinear topological boundary mode arises when the mode amplitude remains below the critical transition amplitude $A_c = \sqrt{-(c_1 + c_2 - c_3)/(d_1 + d_2 - d_3)}$. In our numerics, we choose the parameters as $c_1 = 1$, $d_1 = 4$, $c_2 = 2$, $d_2 = 1.5$, $c_3 = 4$, and $d_3 = 1$.

Figure 4 investigates the zigzag open boundary of the honeycomb lattice. Below this critical phase transition amplitude ($A < A_c$), nonlinear topological boundary modes can emerge along the zigzag lattice boundary, and these modes remain static in time. However, for mode amplitudes $A > A_c$, such nonlinear topological boundary modes cannot arise on the lattice boundary. The reason of nonlinear topological phase transition lies in the behavior near the critical value: when the amplitudes of the nonlinear boundary mode reach the critical value $A = A_c$, the static boundary mode evolves into a static nonlinear bulk mode. This transition signifies the closing of the nonlinear band structure, corresponding to the nonlinear topological phase transition. Consequently, the nonlinear Berry phase, quantized by the chiral symmetry, takes the value of $\gamma(A < A_c) = \pi$ for amplitudes below the transition point and $\gamma(A > A_c) = 0$ for amplitudes above it.

However, the behavior of the nonlinear lattice changes significantly when subjected to *armchair open boundary conditions*. The honeycomb lattice, inherently incompatible with armchair boundaries, necessitates an enlargement of the unit cell from a 4-site lattice to a 16-site lattice (as depicted in figure 5(a)). In this modified configuration, nonlinear static boundary modes can still emerge along the open boundaries of the lattice, provided that the mode amplitudes exceed the topological phase transition amplitude derived for the original 4-site honeycomb lattice (denoted as A_c). In summary, the existence of nonlinear boundary modes (illustrated in figure 5(c)) highlights the dependence of nonlinear boundary mode emergence on the specific choice of open boundary direction.

7. Experimental proposals of chiral-symmetric nonlinear dynamics

Nonlinear Topological Photonics — Chiral-symmetric nonlinear topological physics has been widely studied in photonic systems based on the framework of nonlinear Schrödinger equation [27, 49, 100]. This model excludes second and third harmonic generations to maintain $\mathbf{U}(1)$-symmetry. However, when higher-order harmonics are considered, the topological properties of nonlinear photonics remains unexplored.

Our theory suggests that even with higher harmonics included, chiral symmetry persists in nonlinear photonics. The nonlinear Berry phase remains quantized, and nonlinear topological boundary modes persist. Therefore, chiral-symmetric nonlinear topological physics can be experimentally realized in photonic structures. To achieve this, researchers can intentionally include second and third harmonic generation, thereby breaking the $\mathbf{U}(1)$-symmetry.

Active Electrical Circuit Systems—Recently, an independent experiment involving active electrical circuit metamaterials [113] observed nonlinear topological boundary modes under chiral symmetry. Our work provides theoretical demonstrations of the chiral symmetry and quantized nonlinear Berry phase that align with this real-world experiment.

Bose–Einstein Condensates —[55] explored nonlinear topological physics using the Lotka–Volterra model. This model is crucial for studying boson condensation in driven-dissipative setups [55, 76, 77]. By placing bosons on a lattice structure, the probability distribution of bosons follows the Lotka–Volterra nonlinear model. Such system can be realized experimentally in artificial quantum setups (e.g. superconducting and optical circuits).

8. Conclusions and outlook

In this work, we extend the two non-spatial symmetries, including particle-hole symmetry and chiral symmetry, to nonlinear dynamics whose nonlinear wave functions do not necessarily possess $\mathbf{U}(1)$-gauge symmetry. Chiral symmetry can quantize the Berry phase of nonlinear normal modes, determining their topological phases, and facilitating the emergence of nonlinear topological boundary modes. These modes have pinned frequencies at zero. They exhibit high stability against disruptions in spatial symmetries. Our work enables the non-spatial classification of nonlinear systems, expanding the ten-fold classification of linear topological insulators [103]. Our findings may suggest potential applications in nonlinear dynamics, where the stability conferred by nonlinear topology could aid in resilience against parameter changes.

Data availability statement

The data that support the findings of this study are openly available at the following URL/DOI: https://github.com/kQqr.

Acknowledgment

D Z would like to thank insightful discussions with Anthony J Leggett, Xueda Wen, Junyi Zhang and Feng Li. D Z is supported by the National Natural Science Foundation of China (Grant Nos. 12374157 and 12102039).

Note added. Recently, we became aware of a related independent effort on the chiral symmetry of nonlinear dynamics [113].

Appendix A. Adiabatic geometric phases for nonlinear systems that break U(1)-symmetry

In this section, we derive the adiabatic geometric phase of nonlinear normal modes. We consider the nonlinear equations of motion in a translationally invariant lattice, with $\mathrm{i}\partial_t\Psi(t) = H(\Psi)$, in which the plane-wave nonlinear normal mode reads $\Psi_{\boldsymbol{k}}(\boldsymbol{k}\cdot\boldsymbol{r} - \omega t)$. We consider an adiabatic evolution to the nonlinear mode by slowly changing the wavevector $\boldsymbol{k}$ that follows a closed-loop trajectory in the Brillouin zone. Under the evolution, the nonlinear wave takes the format of

$$\Psi = \Psi_{\boldsymbol{k}}\left(-\int^{t}\omega(t')\,\mathrm{d}t' - \gamma(t)\right) \tag{A1}$$

where $\gamma(t)$ is the adiabatic geometric phase that arises from the temporal evolution. This mode should satisfy the nonlinear equations of motion, which leads to

$$\mathrm{i}\partial_t\Psi = \mathrm{i}\left[\frac{\partial\Psi_{\boldsymbol{k}}}{\partial\boldsymbol{k}}\frac{\mathrm{d}\boldsymbol{k}}{\mathrm{d}t} - \left(\omega + \frac{\mathrm{d}\gamma}{\mathrm{d}t}\right)\frac{\partial\Psi_{\boldsymbol{k}}}{\partial\theta} + \partial_t\delta\Psi\right], \tag{A2}$$

where $\delta\Psi = \Psi - \Psi_{\boldsymbol{k}}$ denotes mode change, and $\theta = \int^t \omega(t')\mathrm{d}t' + \gamma(t)$ denotes the phase variable of the nonlinear mode. Since the shape of the nonlinear mode can vary during the process of adiabatic evolution, the nonlinear Hamiltonian also changes in this adiabatic process, leading to the expansion of the nonlinear Hamiltonian in terms of the mode variation $\delta\Psi$:

$$H(\Psi) = H(\Psi_{\boldsymbol{k}}) + \left(\delta\Psi\frac{\partial H}{\partial\Psi} + \delta\Psi^*\frac{\partial H}{\partial\Psi^*}\right)_{\Psi_{\boldsymbol{k}}}. \tag{A3}$$

Employing the relationship $-\mathrm{i}\omega\partial_\theta\Psi_{\boldsymbol{k}} = H(\Psi_{\boldsymbol{k}})$, we combine equations (A2), (A3) and obtain the equations of motion for the nonlinear mode, which read

$$\frac{\partial\Psi_{\boldsymbol{k}}}{\partial\theta}\frac{\mathrm{d}\gamma}{\mathrm{d}t} = \frac{\partial\Psi_{\boldsymbol{k}}}{\partial\boldsymbol{k}}\frac{\mathrm{d}\boldsymbol{k}}{\mathrm{d}t} + \mathrm{i}\left(\delta\Psi\frac{\partial H}{\partial\Psi} + \delta\Psi^*\frac{\partial H}{\partial\Psi^*} - \mathrm{i}\partial_t\delta\Psi\right)_{\Psi_{\boldsymbol{k}}}. \tag{A4}$$

Equation (A4) contains two terms on the right-hand side. The first term corresponds to the Berry phase of nonlinear normal modes in nonlinear normal modes. The second term arises from the change in the mode shape and amplitude due to the adiabatic evolution, which can affect the nonlinear Hamiltonian of the system. Together, these terms contribute to the overall adiabatic geometric phase of the nonlinear normal modes.

To gain a more detailed understanding of the nonlinear normal mode, we express it in terms of a Fourier series. Specifically, we write $\Psi_{\boldsymbol{k}}(\theta) = \sum_l(\psi_{l\boldsymbol{k}}^{(1)}, \psi_{l\boldsymbol{k}}^{(2)}\mathrm{e}^{\mathrm{i}l\phi_{\boldsymbol{k}}})^\top\mathrm{e}^{\mathrm{i}l\theta}$, where $\psi_{l\boldsymbol{k}}^{(1)}$ and $\psi_{l\boldsymbol{k}}^{(2)}$ are the Fourier components of the mode in the two wave components, respectively, and $\phi_{\boldsymbol{k}}$ is the relative phase between the two components. Thus, we obtain

$$\begin{aligned}\frac{\partial\Psi_{\boldsymbol{k}}}{\partial\theta} &= \sum_l\left(\psi_{l\boldsymbol{k}}^{(1)}, \psi_{l\boldsymbol{k}}^{(2)}\mathrm{e}^{\mathrm{i}l\phi_{\boldsymbol{k}}}\right)^\top \mathrm{i}l\mathrm{e}^{\mathrm{i}l\theta},\\ \frac{\partial\Psi_{\boldsymbol{k}}}{\partial\boldsymbol{k}} &= \sum_l\left[\frac{\partial\psi_{l\boldsymbol{k}}^{(1)}}{\partial\boldsymbol{k}}, \left(\frac{\partial\psi_{l\boldsymbol{k}}^{(2)}}{\partial\boldsymbol{k}} + \mathrm{i}l\psi_{l\boldsymbol{k}}^{(2)}\frac{\partial\phi_{\boldsymbol{k}}}{\partial\boldsymbol{k}}\right)\mathrm{e}^{\mathrm{i}l\phi_{\boldsymbol{k}}}\right]^\top \mathrm{e}^{\mathrm{i}l\theta}.\end{aligned} \tag{A5}$$

We now use equation (A5) to substitute results into equation (A4). We then multiply both sides of equation (A4) by $\Psi_{\boldsymbol{k},\omega}^\dagger$ and integrate over the phase variable θ from 0 to 2π. This procedure leads us to derive the following relationship:

$$\begin{aligned}\frac{\mathrm{d}\gamma}{\mathrm{d}t}\sum_{lj} l|\psi_{l\boldsymbol{k}}^{(i)}|^2 = \frac{\mathrm{d}\boldsymbol{k}}{\mathrm{d}t}\sum_l\left(l\frac{\partial\phi_{\boldsymbol{k}}}{\partial\boldsymbol{k}}|\psi_{l\boldsymbol{k}}^{(2)}|^2 - \mathrm{i}\sum_j\psi_{l\boldsymbol{k}}^{(j)*}\frac{\partial\psi_{l\boldsymbol{k}}^{(i)}}{\partial\boldsymbol{k}}\right)\\ + \int_0^{2\pi}\frac{\mathrm{d}\theta}{2\pi}\Psi_{\boldsymbol{k}}^\dagger\left(\delta\Psi\frac{\partial H}{\partial\Psi} + \delta\Psi^*\frac{\partial H}{\partial\Psi^*} - H(\Psi)\delta\Psi\right)_{\Psi=\Psi_{\boldsymbol{k}}}\end{aligned} \tag{A6}$$

where the relationship $\mathrm{i}\partial_t\delta\Psi = H(\Psi)\delta\Psi$ has been adopted. Finally, we integrate over the time variable t and obtain the Berry phase of nonlinear normal modes:

$$\gamma_C = \gamma_C^{(\mathrm{B})} + \gamma_C^{(\mathrm{NL})}. \tag{A7}$$

In equation (A7), there are two contributions in the adiabatic geometric phase. The first term is the Berry phase of nonlinear normal modes,

$$\gamma_C^{(\mathrm{B})} = \oint_C \mathrm{d}\boldsymbol{k}\frac{\sum_l\left(l\frac{\partial\phi_{\boldsymbol{k}}}{\partial\boldsymbol{k}}|\psi_{l\boldsymbol{k}}^{(2)}|^2 - \mathrm{i}\sum_j\psi_{l\boldsymbol{k}}^{(j)*}\frac{\partial\psi_{l\boldsymbol{k}}^{(i)}}{\partial\boldsymbol{k}}\right)}{\sum_l l\sum_j|\psi_{l\boldsymbol{k}}^{(i)}|^2}. \tag{A8}$$

The second term

$$\gamma_C^{(\mathrm{NL})} = \int\mathrm{d}t\left(\sum_l l\sum_j|\psi_{l\boldsymbol{k}}^{(i)}|^2\right)^{-1}\int_0^{2\pi}\frac{\mathrm{d}\theta}{2\pi}\Psi_{\boldsymbol{k}}^\dagger\left(\delta\Psi\frac{\partial H}{\partial\Psi} + \delta\Psi^*\frac{\partial H}{\partial\Psi^*} - H(\Psi)\delta\Psi\right)_{\Psi=\Psi_{\boldsymbol{k}}} \tag{A9}$$

is known as the 'purely nonlinear' contribution to the adiabatic geometric phase, as it arises solely from the nonlinear interactions within the system. Specifically, it represents the change in the nonlinear Hamiltonian with respect to the variation of the nonlinear normal mode, which arises due to the dependence of the Hamiltonian on the mode amplitude. We emphasize that this term vanishes for the purely linear Schödinger-type equations. The change in the wave function can be expressed in terms of the change in the mode amplitude,

$$\delta\Psi = \frac{\delta A}{A}\Psi, \qquad \delta\Psi^* = \frac{\delta A}{A}\Psi^*, \tag{A10}$$

where $A = \max(\mathrm{Re}\,\Psi)$ is the mode amplitude, and δA is the change in the mode amplitude under adiabatic evolutions. The change of wave function can be expressed in the form of equation (A10), is because that the change in the wave function can stem from two sources: the change in the waveform, and the change in the mode amplitude. The change of waveform has been addressed in equation (A5), where higher-order Fourier series capture the change in the waveform. As a result, the change in the mode amplitude is captured by equation (A10), which is manifested in the term δA.

Because chiral symmetry demands that the mode amplitude should not change and stays invariant during the entire process of adiabatic evolution, we have $\delta A = 0$, and the 'purely nonlinear' contribution to the adiabatic geometric phase should vanish under the constraint of chiral symmetry.

Appendix B. Adiabatic geometric phases for nonlinear systems that respect U(1)-symmetry

In this section, we use the results of the adiabatic geometric phases derived in equations (A8) and (A9) to study the geometric phases for nonlinear systems that respect **U(1)**-symmetry. Our purpose is to verify that our results are consistent with the precedented results derived from nonlinear dynamics that respect **U**(1)-gauge symmetry. Therefore, we consider the Hamiltonian for the nonlinear Schrödinger equations that respect the **U(1)**-gauge symmetry in the wave functions, which is given by

$$H(\Psi) = H_0\Psi + g|\Psi|^2\Psi. \tag{B1}$$

Here, for the two-band model, such as the one discussed in equation (1) of the main text, H_0 is a 2×2 matrix, and g is the coefficient of the nonlinearity. In these systems, the nonlinear normal modes can be represented by sinusoidal waves,

$$\Psi_{\boldsymbol{k}}(\boldsymbol{k}\cdot\boldsymbol{r}-\omega t) = \Psi_{\boldsymbol{k}}e^{i(\boldsymbol{k}\cdot\boldsymbol{r}-\omega t)} = \left(\Psi_{\boldsymbol{k}}^{(1)}, \Psi_{\boldsymbol{k}}^{(2)}e^{i\phi_{\boldsymbol{k}}}\right)^{\top} e^{i(\boldsymbol{k}\cdot\boldsymbol{r}-\omega t)}. \tag{B2}$$

Here, the normalization condition given by $|\Psi_{\boldsymbol{k}}^{(1)}|^2 + |\Psi_{\boldsymbol{k}}^{(2)}|^2 = 1$ has been adopted.

To simplify the Berry phase of nonlinear normal modes, $\gamma_C^{(\mathrm{B})}$, and the purely nonlinear contribution to the adiabatic geometric phase, $\gamma_C^{(\mathrm{NL})}$, we employ the relationships given by the representation of nonlinear normal modes as sinusoidal waves, as presented in equation (B2). In particular, we note that nonlinear plane waves in these systems contain only the fundamental harmonic, which allows us to simplify the expressions for $\psi_{l\boldsymbol{k}}^{(1)}$ and $\psi_{l\boldsymbol{k}}^{(2)}$ as $\psi_{l\boldsymbol{k}}^{(1)} = \Psi_{\boldsymbol{k}}^{(1)}\delta_{l1}$ and $\psi_{l\boldsymbol{k}}^{(2)} = \Psi_{\boldsymbol{k}}^{(2)}\delta_{l1}$, respectively. Plugging these simplifications into $\gamma_C^{(\mathrm{B})}$ reduces the Berry phase of nonlinear normal modes as

$$\begin{aligned}
\gamma_C^{(\mathrm{B})} &= \oint_C \mathrm{d}\boldsymbol{k}\cdot \frac{\sum_l \left(l|\psi_{l\boldsymbol{k}}^{(2)}|^2\frac{\partial\phi_{\boldsymbol{k}}}{\partial\boldsymbol{k}} + i\sum_j \psi_{l\boldsymbol{k}}^{(j)*}\frac{\partial\psi_{l\boldsymbol{k}}^{(i)}}{\partial\boldsymbol{k}}\right)\delta_{l1}}{\sum_{l'} l'\left(\sum_{j'}|\psi_{l'\boldsymbol{k}}^{(j')}|^2\right)\delta_{l'1}} = \oint_C \mathrm{d}\boldsymbol{k}\cdot\left(|\psi_{1\boldsymbol{k}}^{(2)}|^2\frac{\partial\phi_{\boldsymbol{k}}}{\partial\boldsymbol{k}} + i\sum_j \psi_{1\boldsymbol{k}}^{(j)*}\frac{\partial\psi_{1\boldsymbol{k}}^{(i)}}{\partial\boldsymbol{k}}\right)\\
&= \oint_C \mathrm{d}\boldsymbol{k}\cdot i\left(\sum_j \Psi_{\boldsymbol{k}}^{(j)*}\partial_{\boldsymbol{k}}\Psi_{\boldsymbol{k}}^{(i)} - i|\Psi_{\boldsymbol{k}}^{(2)}|^2\partial_{\boldsymbol{k}}\phi_{\boldsymbol{k}}\right) = \oint_C \mathrm{d}\boldsymbol{k}\cdot i\left(\Psi_{\boldsymbol{k}}^{(1)*}, \Psi_{\boldsymbol{k}}^{(2)*}e^{-i\phi_{\boldsymbol{k}}}\right)\partial_{\boldsymbol{k}}\begin{pmatrix}\Psi_{\boldsymbol{k}}^{(1)}\\ \Psi_{\boldsymbol{k}}^{(2)}e^{i\phi_{\boldsymbol{k}}}\end{pmatrix}\\
&= \oint_C \mathrm{d}\boldsymbol{k}\cdot i\langle\Psi_{\boldsymbol{k}}|\partial_{\boldsymbol{k}}|\Psi_{\boldsymbol{k}}\rangle = \gamma_{C,\mathrm{linear}}^{(\mathrm{B})},
\end{aligned} \tag{B3}$$

where $\Psi_{\boldsymbol{k}} = (\Psi_{\boldsymbol{k}}^{(1)}, \Psi_{\boldsymbol{k}}^{(2)}e^{i\phi_{\boldsymbol{k}}})^{\top}$ is the eigenvector of the Hamiltonian, and $\gamma_{C,\mathrm{linear}}^{(\mathrm{B})}$ denotes the conventional form of Berry phase in linear systems. At this point, we have shown that the Berry phase of nonlinear normal modes, as expressed in equation (9), can be reduced to the conventional Berry phase when the nonlinear wave functions yield **U**(1)-gauge symmetry. This result is in perfect agreement with the Berry phase derived in [3].

When considering nonlinear interactions of the form

$$H(\Psi) = H_0\Psi + g|\Psi|^2\Psi, \tag{B4}$$

we can compute the contribution of nonlinear interactions to the adiabatic geometric phase, $\gamma_C^{(\mathrm{NL})}$. By using the relationships $\partial H(\Psi)/\partial\Psi = H_0 + 2g|\Psi|^2$ and $\partial H(\Psi)/\partial\Psi^* = g\Psi^2$, we can substitute into $\gamma_C^{(\mathrm{NL})}$ to obtain the result

$$\begin{aligned}\gamma_C^{(\mathrm{NL})} &= \int \mathrm{d}t \left(\sum_l l \sum_j |\psi_{l\boldsymbol{k}}^{(i)}|^2 \delta_{l1}\right)^{-1} \int_0^{2\pi} \frac{\mathrm{d}\theta}{2\pi} \Psi_{\boldsymbol{k}}^\dagger \left(\delta\Psi \frac{\partial H}{\partial \Psi} + \delta\Psi^* \frac{\partial H}{\partial \Psi^*} - H(\Psi)\delta\Psi\right)_{\Psi_{\boldsymbol{k}}} \\ &= \int \mathrm{d}t \int_0^{2\pi} \frac{\mathrm{d}\theta}{2\pi} \Psi_{\boldsymbol{k}}^\dagger \left(\delta\Psi \frac{\partial H}{\partial \Psi} + \delta\Psi^* \frac{\partial H}{\partial \Psi^*} - H(\Psi)\delta\Psi\right)_{\Psi_{\boldsymbol{k}}} = \int \mathrm{d}t\, g\left(\Psi^2\Psi^\dagger\delta\Psi^\dagger + \Psi^{\dagger 2}\Psi\delta\Psi\right)_{\Psi_{\boldsymbol{k}}}.\end{aligned} \tag{B5}$$

This result is in line with the 'purely nonlinear' geometric phase derived in [95], where the nonlinear interaction with $\mathbf{U}(1)$-symmetry is specified.

Appendix C. Analytical results of nonlinear topological boundary modes

In this section, we analyze the decay rate of the nonlinear boundary mode by setting the static condition, $\partial\Psi_{\boldsymbol{r}}^{(i)}/\partial t = 0$, and simplifying the Schrödinger-type nonlinear equations of motion, as given by

$$\begin{aligned}\Psi_{\boldsymbol{r}}^{(1)} - \sum_{j=x,y} g_j \left(\Psi_{\boldsymbol{r}+\hat{e}_j}^{(1)} + \Psi_{\boldsymbol{r}-\hat{e}_j}^{(1)}\right) - \Psi_{\boldsymbol{r}+\hat{e}_x}^{(2)} + \Psi_{\boldsymbol{r}-\hat{e}_x}^{(2)} = 0, \\ \Psi_{\boldsymbol{r}}^{(2)} - \sum_{j=x,y} g_j \left(\Psi_{\boldsymbol{r}+\hat{e}_j}^{(2)} + \Psi_{\boldsymbol{r}-\hat{e}_j}^{(2)}\right) - \Psi_{\boldsymbol{r}+\hat{e}_x}^{(1)} + \Psi_{\boldsymbol{r}-\hat{e}_x}^{(1)} = 0.\end{aligned} \tag{C1}$$

We analyze the behavior of the nonlinear boundary mode, which is exponentially localized on the left open boundary and takes the form of a plane wave in the transverse y direction. Using this ansatz, we derive the wave amplitudes and substitute from the static motion equations given by equation (C1). The resulting solution, as given by equation (21), provides an analytic expression for the spatial decay rates of the edge mode, which are expressed as

$$\kappa_\pm(k_y) = -\ln\left[\frac{\frac{1}{2} - g_y\cos k_y \pm \sqrt{\left(\frac{1}{2} - g_y\cos k_y\right)^2 + 1 - g_x^2}}{g_x + 1}\right]. \tag{C2}$$

The analytical expression for the spatial decay rates of the nonlinear boundary mode, as given by equation (C2), reveals important insights into the behavior of the mode at different values of the nonlinearity parameters and the transverse wavevector. In particular, we find that within the red region of parameter space in figure 2(a), where $-g_x + 1/2 < g_y < g_x - 1/2 \bigcup g_x + 1/2 < g_y < -g_x - 1/2$, the decay rates are positive, indicating that the mode described by equation (21) is exponentially localized on the left open boundary of the square lattice.

Appendix D. Nonlinear topological physics of honeycomb lattice

The model corresponds to a four-site unit cell honeycomb lattice, where each site is identified by position vectors $\boldsymbol{r}_A(\boldsymbol{n})$, $\boldsymbol{r}_B(\boldsymbol{n})$, $\boldsymbol{r}_C(\boldsymbol{n})$, and $\boldsymbol{r}_D(\boldsymbol{n})$. The specific parameters are detailed in the main text. Subsequently, the nonlinear equations of motion for these lattice sites are expressed as follows:

$$\begin{aligned}\mathrm{i}\partial_t\Psi_{\boldsymbol{r}_A}^{(1)} &= f_1\left(\Psi_{\boldsymbol{r}_A}^{(1)}, \Psi_{\boldsymbol{r}_A+\boldsymbol{l}_1}^{(2)}\right) + f_2\left(\Psi_{\boldsymbol{r}_A}^{(1)}, \Psi_{\boldsymbol{r}_A+\boldsymbol{l}_2}^{(2)}\right) + f_3\left(\Psi_{\boldsymbol{r}_A}^{(1)}, \Psi_{\boldsymbol{r}_A+\boldsymbol{l}_3}^{(4)}\right) \\ \mathrm{i}\partial_t\Psi_{\boldsymbol{r}_B}^{(2)} &= f_1\left(\Psi_{\boldsymbol{r}_B}^{(2)}, \Psi_{\boldsymbol{r}_B-\boldsymbol{l}_1}^{(1)}\right) + f_2\left(\Psi_{\boldsymbol{r}_B}^{(2)}, \Psi_{\boldsymbol{r}_B-\boldsymbol{l}_2}^{(1)}\right) + f_6\left(\Psi_{\boldsymbol{r}_B}^{(2)}, \Psi_{\boldsymbol{r}_B-\boldsymbol{l}_3}^{(3)}\right) \\ \mathrm{i}\partial_t\Psi_{\boldsymbol{r}_C}^{(3)} &= f_4\left(\Psi_{\boldsymbol{r}_C}^{(3)}, \Psi_{\boldsymbol{r}_C+\boldsymbol{l}_1}^{(4)}\right) + f_5(\Psi_{\boldsymbol{r}_C}^{(3)}, \Psi_{\boldsymbol{r}_C+\boldsymbol{l}_2}^{(4)}) + f_6(\Psi_{\boldsymbol{r}_C}^{(3)}, \Psi_{\boldsymbol{r}_C+\boldsymbol{l}_3}^{(2)}) \\ \mathrm{i}\partial_t\Psi_{\boldsymbol{r}_D}^{(4)} &= f_4(\Psi_{\boldsymbol{r}_D}^{(4)}, \Psi_{\boldsymbol{r}_D-\boldsymbol{l}_1}^{(3)}) + f_5(\Psi_{\boldsymbol{r}_D}^{(4)}, \Psi_{\boldsymbol{r}_D-\boldsymbol{l}_2}^{(3)}) + f_3(\Psi_{\boldsymbol{r}_D}^{(4)}, \Psi_{\boldsymbol{r}_D-\boldsymbol{l}_3}^{(1)}).\end{aligned} \tag{D1}$$

In order to have the chiral symmetry in this nonlinear model, we ask that the nonlinear interactions yield

$$f_{i+3}(x,y) = -f_i(x,y) \qquad i = 1,2,3. \tag{D2}$$

Under the constraint of nonlinear interactions, the equations of motion for this nonlinear system remain invariant under the chiral operator transformation. Specifically, when we express the plane-wave ansatz as follows:

$$\Psi_{\boldsymbol{k}} = \left(\Psi_{\boldsymbol{k}}^{(1)}\left(\boldsymbol{k}\cdot\boldsymbol{r}-\omega t-\phi_{\boldsymbol{k}}^{(1)}\right), \Psi_{\boldsymbol{k}}^{(2)}\left(\boldsymbol{k}\cdot\boldsymbol{r}-\omega t-\phi_{\boldsymbol{k}}^{(2)}\right), \Psi_{\boldsymbol{k}}^{(3)}\left(\boldsymbol{k}\cdot\boldsymbol{r}-\omega t-\phi_{\boldsymbol{k}}^{(3)}\right), \Psi_{\boldsymbol{k}}^{(4)}\left(\boldsymbol{k}\cdot\boldsymbol{r}-\omega t-\phi_{\boldsymbol{k}}^{(4)}\right)\right)^{\top}. \tag{D3}$$

Then the nonlinear Hamiltonian, denoted as $H(\Psi)$, remains invariant under the transformation,

$$\mathcal{S}H(\Psi)+H(\mathcal{S}\Psi)=0, \qquad \mathcal{S}=\sigma_x\otimes I_2. \tag{D4}$$

Furthermore, the nonlinear equations of motion remain invariant under the chiral transformation. In other words, given a nonlinear normal mode described by equation (D3), chiral symmetry guarantees the existence of a partner solution:

$$\Psi_{\boldsymbol{k},-} = \mathcal{S}\Psi_{\boldsymbol{k}} = \left(\Psi_{\boldsymbol{k}}^{(3)}\left(\boldsymbol{k}\cdot\boldsymbol{r}+\omega t-\phi_{\boldsymbol{k}}^{(3)}\right), \Psi_{\boldsymbol{k}}^{(4)}\left(\boldsymbol{k}\cdot\boldsymbol{r}+\omega t-\phi_{\boldsymbol{k}}^{(4)}\right), \Psi_{\boldsymbol{k}}^{(1)}\left(\boldsymbol{k}\cdot\boldsymbol{r}+\omega t-\phi_{\boldsymbol{k}}^{(1)}\right), \Psi_{\boldsymbol{k}}^{(2)}\left(\boldsymbol{k}\cdot\boldsymbol{r}+\omega t-\phi_{\boldsymbol{k}}^{(2)}\right)\right)^{\top}. \tag{D5}$$

Next, we compute the Berry phase of nonlinear normal modes for this system. By adiabatically evolving the initial nonlinear normal mode, we find the Berry phase of nonlinear normal modes as:

$$\gamma_C^{(\mathrm{B})} = \oint_C \mathrm{d}\boldsymbol{k}\cdot\frac{\sum_{l=-\infty}^{\infty}\sum_{j=1}^{4}\left(l|\psi_{l,\boldsymbol{k}}^{(j)}|^2\nabla_{\boldsymbol{k}}\phi_{\boldsymbol{k}}^{(j)}+\mathrm{i}\psi_{l,\boldsymbol{k}}^{(j)*}\nabla_{\boldsymbol{k}}\psi_{l,\boldsymbol{k}}^{(j)}\right)}{\sum_{l'=-\infty}^{\infty}\sum_{j'=1,2,3,4}l'|\psi_{l',\boldsymbol{k}}^{(j')}|^2} \qquad \mathrm{mod}\ 2\pi. \tag{D6}$$

Then, we adiabatically evolve the chiral-partner mode, via the generalized nonlinear Schrödinger equation, $\mathrm{i}\partial_t\Psi_{\boldsymbol{k},-}=H(\Psi_{\boldsymbol{k},-})$. This evolution gives us the geometric phase: $\Psi(t)=\Psi_{\boldsymbol{k}(t),-\omega}\left(\int_0^t\omega(t',\boldsymbol{k}(t'))+\gamma(t)\right)$. After completing the closed-loop trajectory in reciprocal space, we have:

$$\gamma_C^{(\mathrm{B})} = -\oint_C \mathrm{d}\boldsymbol{k}\cdot\frac{\sum_{l=-\infty}^{\infty}\sum_{j=3,4,1,2}\left(l|\psi_{l,\boldsymbol{k}}^{(j)}|^2\nabla_{\boldsymbol{k}}\phi_{\boldsymbol{k}}^{(j)}+\mathrm{i}\psi_{l,\boldsymbol{k}}^{(j)*}\nabla_{\boldsymbol{k}}\psi_{l,\boldsymbol{k}}^{(j)}\right)}{\sum_{l'=-\infty}^{\infty}\sum_{j'=3,4,1,2}l'|\psi_{l',\boldsymbol{k}}^{(j')}|^2} \qquad \mathrm{mod}\ 2\pi. \tag{D7}$$

Because equations (D6) and (D8) represent the same geometric phase, we equate them, and obtain

$$\gamma_C^{(\mathrm{B})} = n\pi \qquad \mathrm{mod}\ 2\pi. \tag{D8}$$

These quantized integer values indicate that the Berry phase of nonlinear normal modes serves as the topological index of the nonlinear dynamics. Specifically, if there is a nonlinear edge mode localized on the *zigzag* boundary of the honeycomb lattice and the mode remains static in time, then this mode must be topologically protected. In what follows, we explore the nonlinear topological boundary modes for two different boundary conditions in the honeycomb lattice: the *zigzag open boundary condition* and the *armchair open boundary condition*.

D.1. Nonlinear topological modes for zigzag open boundary conditions

As depicted in figure 4, the zigzag boundary condition aligns seamlessly with the lattice configuration of the honeycomb lattice. By imposing the static condition:

$$\partial_t\Psi_{\boldsymbol{r}_X}^{(j)}=0, \qquad X=A,B,C,D, \qquad j=1,2,3,4. \tag{D9}$$

we obtain static nonlinear boundary modes. These modes are governed by the following nonlinear recursion relations:

$$\begin{aligned}
&f_1\left(\Psi_{\boldsymbol{r}_A}^{(1)},\Psi_{\boldsymbol{r}_A+\boldsymbol{l}_1}^{(2)}\right)+f_2\left(\Psi_{\boldsymbol{r}_A}^{(1)},\Psi_{\boldsymbol{r}_A+\boldsymbol{l}_2}^{(2)}\right)+f_3\left(\Psi_{\boldsymbol{r}_A}^{(1)},\Psi_{\boldsymbol{r}_A+\boldsymbol{l}_3}^{(4)}\right)=\mathrm{i}\partial_t\Psi_{\boldsymbol{r}_A}^{(1)}=0\\
&f_1\left(\Psi_{\boldsymbol{r}_B}^{(2)},\Psi_{\boldsymbol{r}_B-\boldsymbol{l}_1}^{(1)}\right)+f_2\left(\Psi_{\boldsymbol{r}_B}^{(2)},\Psi_{\boldsymbol{r}_B-\boldsymbol{l}_2}^{(1)}\right)-f_3\left(\Psi_{\boldsymbol{r}_B}^{(2)},\Psi_{\boldsymbol{r}_B-\boldsymbol{l}_3}^{(3)}\right)=\mathrm{i}\partial_t\Psi_{\boldsymbol{r}_B}^{(2)}=0\\
&f_1\left(\Psi_{\boldsymbol{r}_C}^{(3)},\Psi_{\boldsymbol{r}_C+\boldsymbol{l}_1}^{(4)}\right)+f_2\left(\Psi_{\boldsymbol{r}_C}^{(3)},\Psi_{\boldsymbol{r}_C+\boldsymbol{l}_2}^{(4)}\right)+f_3(\Psi_{\boldsymbol{r}_C}^{(3)},\Psi_{\boldsymbol{r}_C+\boldsymbol{l}_3}^{(2)})=\mathrm{i}\partial_t\Psi_{\boldsymbol{r}_C}^{(3)}=0\\
&f_1(\Psi_{\boldsymbol{r}_D}^{(4)},\Psi_{\boldsymbol{r}_D-\boldsymbol{l}_1}^{(3)})+f_2(\Psi_{\boldsymbol{r}_D}^{(4)},\Psi_{\boldsymbol{r}_D-\boldsymbol{l}_2}^{(3)})-f_3(\Psi_{\boldsymbol{r}_D}^{(4)},\Psi_{\boldsymbol{r}_D-\boldsymbol{l}_3}^{(1)})=\mathrm{i}\partial_t\Psi_{\boldsymbol{r}_D}^{(4)}=0.
\end{aligned} \tag{D10}$$

Additionally, we impose an open boundary condition:

$$f_1\left(\Psi^{(2)}_{\boldsymbol{r}_B},\Psi^{(1)}_{\boldsymbol{r}_B-\boldsymbol{l}_1}\right)+f_2\left(\Psi^{(2)}_{\boldsymbol{r}_B},\Psi^{(1)}_{\boldsymbol{r}_B-\boldsymbol{l}_2}\right)=\mathrm{i}\partial_t\Psi^{(2)}_{\boldsymbol{r}_B}=0 \qquad \text{for} \quad n_1=0. \tag{D11}$$

In this context, we illustrate a specific nonlinear topological boundary mode in the nonlinear honeycomb lattice, where we set $\Psi^{(j)}_{\boldsymbol{r}}=\Psi^{(j)}_{\boldsymbol{r}\pm\boldsymbol{a}_2}$. Numerical solutions reveal the temporal stability of this nonlinear boundary mode, which can persist indefinitely.

The emergence of nonlinear topological boundary modes in the honeycomb lattice hinges on a critical condition related to the mode amplitude. Specifically, these modes cannot arise at the lattice boundary when the mode amplitude, denoted as $A=\max(\mathrm{Re}\,\Psi^{(2)}_{\boldsymbol{r}})$, exceeds the critical value

$$A_c=\sqrt{-\frac{c_1+c_2-c_3}{d_1+d_2-d_3}}. \tag{D12}$$

When the mode amplitude exceeds the critical value (such as $(A>A_c)$), as indicated by the analytical nonlinear recursion relation in equation (D10), the mode undergoes exponential growth into the lattice. This nonlinear mode cannot be initialized and remains unlocalized on the open boundary. Importantly, at this critical amplitude, the static nonlinear mode neither decays nor shrinks in space. Instead, it assumes the character of a nonlinear bulk mode. When the mode amplitude drops below the critical value, a localized nonlinear topological mode emerges on the lattice open boundary. This critical behavior corresponds to a nonlinear topological phase transition. Specifically, for mode amplitudes below the critical threshold $(A<A_c)$, the nonlinear topological index takes the value $(\gamma(A<A_c)=\pi)$. Conversely, for mode amplitudes above the critical threshold $(A>A_c)$, the nonlinear topological index becomes $(\gamma(A>A_c)=0)$. Conversely, for mode amplitudes above the critical threshold $(A>A_c)$, the nonlinear topological index becomes $(\gamma(A>A_c)=0)$.

D.2. Nonlinear boundary modes for armchair open boundary condition

When we examine the armchair open boundary conditions, we encounter an incompatibility with the initial definition of the honeycomb lattice. As illustrated in figure 5, the lattice structure necessitates redefinition, resulting in an enlarged unit cell: expanding from the original four-site unit cell to a larger 16-site unit cell. In this revised configuration, we label the sites within the unit cell as follows: $A^{(j)}$, $B^{(j)}$, $C^{(j)}$, and $D^{(j)}$ with $j=0,1,2,3$. The corresponding wave functions associated with these sites are denoted as: $\Psi^{(1,j)}_{\boldsymbol{r}}$, $\Psi^{(2,j)}_{\boldsymbol{r}}$, $\Psi^{(3,j)}_{\boldsymbol{r}}$, and $\Psi^{(4,j)}_{\boldsymbol{r}}$. This redefined lattice configuration introduces new primitive vectors, which we now define as

$$\boldsymbol{a}_1'=-4\boldsymbol{l}_1+2\boldsymbol{l}_2+2\boldsymbol{l}_3=6\ell\,(0,1)\,, \qquad \boldsymbol{a}_2'=-2\boldsymbol{l}_2+2\boldsymbol{l}_3=2\sqrt{3}\ell\,(1,0)\,. \tag{D13}$$

The position of the unit cell is given by $\boldsymbol{r}(\boldsymbol{n})=n_1\boldsymbol{a}_1'+n_2\boldsymbol{a}_2'$. For each site within the unit cell (labeled as $X^{(j)}=A^{(j)},B^{(j)},C^{(j)},D^{(j)}$, the site position becomes: $\boldsymbol{r}_{X^{(j)}}(\boldsymbol{n})=n_1\boldsymbol{a}_1'+n_2\boldsymbol{a}_2'+\boldsymbol{r}^{(j)}_X$ for $X=A,B,C,D$ and $j=0,1,2,3$. Now, let us delve into the equations of motion associated with this redefined lattice configuration. For the $A^{(j)}$ sites,

$$\begin{aligned}
\mathrm{i}\partial_t\Psi^{(1,0)}_{\boldsymbol{r}}&=f_1\left(\Psi^{(1,0)}_{\boldsymbol{r}},\Psi^{(2,0)}_{\boldsymbol{r}}\right)+f_2\left(\Psi^{(1,0)}_{\boldsymbol{r}},\Psi^{(2,1)}_{\boldsymbol{r}}\right)+f_3\left(\Psi^{(1,0)}_{\boldsymbol{r}},\Psi^{(4,1)}_{\boldsymbol{r}}\right)\\
\mathrm{i}\partial_t\Psi^{(1,1)}_{\boldsymbol{r}}&=f_1\left(\Psi^{(1,1)}_{\boldsymbol{r}},\Psi^{(2,1)}_{\boldsymbol{r}}\right)+f_2\left(\Psi^{(1,1)}_{\boldsymbol{r}},\Psi^{(2,2)}_{\boldsymbol{r}}\right)+f_3\left(\Psi^{(1,1)}_{\boldsymbol{r}},\Psi^{(4,2)}_{\boldsymbol{r}}\right)\\
\mathrm{i}\partial_t\Psi^{(1,2)}_{\boldsymbol{r}}&=f_1\left(\Psi^{(1,2)}_{\boldsymbol{r}},\Psi^{(2,2)}_{\boldsymbol{r}}\right)+f_2(\Psi^{(1,2)}_{\boldsymbol{r}},\Psi^{(2,3)}_{\boldsymbol{r}})+f_3(\Psi^{(1,2)}_{\boldsymbol{r}},\Psi^{(4,3)}_{\boldsymbol{r}})\\
\mathrm{i}\partial_t\Psi^{(1,3)}_{\boldsymbol{r}}&=f_1(\Psi^{(1,3)}_{\boldsymbol{r}},\Psi^{(2,3)}_{\boldsymbol{r}})+f_2(\Psi^{(1,3)}_{\boldsymbol{r}},\Psi^{(2,0)}_{\boldsymbol{r}+\boldsymbol{a}_1'-\boldsymbol{a}_2'})+f_3(\Psi^{(1,3)}_{\boldsymbol{r}},\Psi^{(4,0)}_{\boldsymbol{r}+\boldsymbol{a}_1'-\boldsymbol{a}_2'});
\end{aligned} \tag{D14}$$

for the $B^{(j)}$ sites:

$$\begin{aligned}
\mathrm{i}\partial_t\Psi^{(2,0)}_{\boldsymbol{r}}&=f_1\left(\Psi^{(2,0)}_{\boldsymbol{r}},\Psi^{(1,0)}_{\boldsymbol{r}}\right)+f_2\left(\Psi^{(2,0)}_{\boldsymbol{r}},\Psi^{(1,3)}_{\boldsymbol{r}-\boldsymbol{a}_1'}\right)+f_6\left(\Psi^{(2,0)}_{\boldsymbol{r}},\Psi^{(3,3)}_{\boldsymbol{r}-\boldsymbol{a}_1'-\boldsymbol{a}_2'}\right)\\
\mathrm{i}\partial_t\Psi^{(2,1)}_{\boldsymbol{r}}&=f_1\left(\Psi^{(2,1)}_{\boldsymbol{r}},\Psi^{(1,1)}_{\boldsymbol{r}}\right)+f_2\left(\Psi^{(2,1)}_{\boldsymbol{r}},\Psi^{(1,0)}_{\boldsymbol{r}_B}\right)+f_6\left(\Psi^{(2,1)}_{\boldsymbol{r}},\Psi^{(3,0)}_{\boldsymbol{r}-\boldsymbol{a}_2'}\right)\\
\mathrm{i}\partial_t\Psi^{(2,2)}_{\boldsymbol{r}}&=f_1\left(\Psi^{(2,2)}_{\boldsymbol{r}},\Psi^{(1,2)}_{\boldsymbol{r}}\right)+f_2(\Psi^{(2,2)}_{\boldsymbol{r}},\Psi^{(1,1)}_{\boldsymbol{r}})+f_6(\Psi^{(2,2)}_{\boldsymbol{r}},\Psi^{(3,1)}_{\boldsymbol{r}-\boldsymbol{a}_2'})\\
\mathrm{i}\partial_t\Psi^{(2,3)}_{\boldsymbol{r}}&=f_1(\Psi^{(2,3)}_{\boldsymbol{r}},\Psi^{(1,3)}_{\boldsymbol{r}})+f_2(\Psi^{(2,3)}_{\boldsymbol{r}},\Psi^{(1,2)}_{\boldsymbol{r}})+f_6(\Psi^{(2,3)}_{\boldsymbol{r}},\Psi^{(3,2)}_{\boldsymbol{r}-\boldsymbol{a}_2'});
\end{aligned} \tag{D15}$$

for the $C^{(j)}$ sites:

$$\begin{aligned}
\mathrm{i}\partial_t\Psi_{\boldsymbol{r}}^{(3,0)} &= f_4\left(\Psi_{\boldsymbol{r}}^{(3,0)},\Psi_{\boldsymbol{r}}^{(4,0)}\right)+f_5\left(\Psi_{\boldsymbol{r}}^{(3,0)},\Psi_{\boldsymbol{r}}^{(4,1)}\right)+f_6\left(\Psi_{\boldsymbol{r}}^{(3,0)},\Psi_{\boldsymbol{r}+\boldsymbol{a}_2'}^{(2,1)}\right)\\
\mathrm{i}\partial_t\Psi_{\boldsymbol{r}_C}^{(3,1)} &= f_4\left(\Psi_{\boldsymbol{r}_C}^{(3,1)},\Psi_{\boldsymbol{r}}^{(4,1)}\right)+f_5\left(\Psi_{\boldsymbol{r}_C}^{(3,1)},\Psi_{\boldsymbol{r}}^{(4,2)}\right)+f_6\left(\Psi_{\boldsymbol{r}_C}^{(3,1)},\Psi_{\boldsymbol{r}+\boldsymbol{a}_2'}^{(2,2)}\right)\\
\mathrm{i}\partial_t\Psi_{\boldsymbol{r}_C}^{(3,2)} &= f_4\left(\Psi_{\boldsymbol{r}_C}^{(3,2)},\Psi_{\boldsymbol{r}}^{(4,2)}\right)+f_5(\Psi_{\boldsymbol{r}_C}^{(3,2)},\Psi_{\boldsymbol{r}}^{(4,3)})+f_6(\Psi_{\boldsymbol{r}_C}^{(3,2)},\Psi_{\boldsymbol{r}+\boldsymbol{a}_2'}^{(2,3)})\\
\mathrm{i}\partial_t\Psi_{\boldsymbol{r}}^{(3,3)} &= f_4(\Psi_{\boldsymbol{r}}^{(3,3)},\Psi_{\boldsymbol{r}}^{(4,3)})+f_5(\Psi_{\boldsymbol{r}}^{(3,3)},\Psi_{\boldsymbol{r}+\boldsymbol{a}_1'-\boldsymbol{a}_2'}^{(4,0)})+f_6(\Psi_{\boldsymbol{r}}^{(3,3)},\Psi_{\boldsymbol{r}+\boldsymbol{a}_1'}^{(2,0)});
\end{aligned}\tag{D16}$$

for the $D^{(j)}$ sites:

$$\begin{aligned}
\mathrm{i}\partial_t\Psi_{\boldsymbol{r}}^{(4,0)} &= f_4\left(\Psi_{\boldsymbol{r}}^{(4,0)},\Psi_{\boldsymbol{r}}^{(3,0)}\right)+f_5\left(\Psi_{\boldsymbol{r}}^{(4,0)},\Psi_{\boldsymbol{r}-\boldsymbol{a}_1'}^{(3,3)}\right)+f_3\left(\Psi_{\boldsymbol{r}}^{(4,0)},\Psi_{\boldsymbol{r}-\boldsymbol{a}_1'}^{(1,3)}\right)\\
\mathrm{i}\partial_t\Psi_{\boldsymbol{r}}^{(4,1)} &= f_4\left(\Psi_{\boldsymbol{r}}^{(4,1)},\Psi_{\boldsymbol{r}}^{(3,1)}\right)+f_5\left(\Psi_{\boldsymbol{r}}^{(4,1)},\Psi_{\boldsymbol{r}}^{(3,0)}\right)+f_3\left(\Psi_{\boldsymbol{r}}^{(4,1)},\Psi_{\boldsymbol{r}}^{(1,0)}\right)\\
\mathrm{i}\partial_t\Psi_{\boldsymbol{r}}^{(4,2)} &= f_4\left(\Psi_{\boldsymbol{r}}^{(4,2)},\Psi_{\boldsymbol{r}}^{(3,2)}\right)+f_5(\Psi_{\boldsymbol{r}}^{(4,2)},\Psi_{\boldsymbol{r}}^{(3,1)})+f_3(\Psi_{\boldsymbol{r}}^{(4,2)},\Psi_{\boldsymbol{r}}^{(1,1)})\\
\mathrm{i}\partial_t\Psi_{\boldsymbol{r}}^{(4,3)} &= f_4(\Psi_{\boldsymbol{r}}^{(4,3)},\Psi_{\boldsymbol{r}}^{(3,3)})+f_5(\Psi_{\boldsymbol{r}}^{(4,3)},\Psi_{\boldsymbol{r}}^{(3,2)})+f_3(\Psi_{\boldsymbol{r}}^{(4,3)},\Psi_{\boldsymbol{r}}^{(1,2)})
\end{aligned}\tag{D17}$$

The armchair open boundary condition reads

$$\begin{aligned}
\mathrm{i}\partial_t\Psi_{\boldsymbol{r}}^{(1,3)} &= f_1\left(\Psi_{\boldsymbol{r}}^{(1,3)},\Psi_{\boldsymbol{r}}^{(2,3)}\right)+f_3\left(\Psi_{\boldsymbol{r}}^{(1,3)},\Psi_{\boldsymbol{r}+\boldsymbol{a}_1'-\boldsymbol{a}_2'}^{(4,0)}\right)\\
\mathrm{i}\partial_t\Psi_{\boldsymbol{r}}^{(2,3)} &= f_1\left(\Psi_{\boldsymbol{r}}^{(2,3)},\Psi_{\boldsymbol{r}}^{(1,3)}\right)+f_2\left(\Psi_{\boldsymbol{r}}^{(2,3)},\Psi_{\boldsymbol{r}}^{(1,2)}\right)\\
\mathrm{i}\partial_t\Psi_{\boldsymbol{r}_C}^{(3,1)} &= f_4\left(\Psi_{\boldsymbol{r}_C}^{(3,1)},\Psi_{\boldsymbol{r}}^{(4,1)}\right)+f_6\left(\Psi_{\boldsymbol{r}_C}^{(3,1)},\Psi_{\boldsymbol{r}+\boldsymbol{a}_2'}^{(2,2)}\right)\\
\mathrm{i}\partial_t\Psi_{\boldsymbol{r}}^{(4,1)} &= f_4\left(\Psi_{\boldsymbol{r}}^{(4,1)},\Psi_{\boldsymbol{r}}^{(3,1)}\right)+f_5(\Psi_{\boldsymbol{r}}^{(4,1)},\Psi_{\boldsymbol{r}}^{(3,0)}).
\end{aligned}\tag{D18}$$

The static condition of the nonlinear boundary mode is obtained by asking

$$\partial_t\Psi_{\boldsymbol{r}}^{(j,j')}=0,\quad \text{for}\quad j=1,2,3,4\qquad j'=0,1,2,3.\tag{D19}$$

Within the framework of nonlinear equations of motion and under the armchair open boundary conditions, a rich variety of nonlinear boundary static modes can emerge. Here, we focus on illustrating one such mode by imposing the condition $\Psi_{\boldsymbol{r}\pm\boldsymbol{a}_1'}^{(j,j')}=\Psi_{\boldsymbol{r}}^{(j,j')}$. This choice leads us to the specific nonlinear boundary mode depicted in figure 5. To explore its behavior, we turn to numerical simulations. Under the armchair boundary condition, a critical amplitude arises:

$$A_c'=0.72\sqrt{-\frac{c_1-c_2-c_3}{d_1-d_2-d_3}}.\tag{D20}$$

The significance of this critical amplitude lies in the fundamental change the boundary condition introduces. First, due to the incompatibility between the armchair open boundary condition and the honeycomb lattice, we must enlarge the lattice's unit cell from the original four-site configuration to a 16-site unit cell. Secondly, the critical amplitude A_c' marks a transition point. Below this threshold ($A<A_c'$), a nonlinear boundary mode localizes on the open surface of the lattice. However, for $A>A_c'$, the nonlinear boundary mode diverges in space when analytically initialized, rendering it forbidden.

Interestingly, the behavior of nonlinear boundary modes depends significantly on the choice of boundary conditions. Under the zigzag boundary condition, the nonlinear topological boundary mode is not allowed to exist when the mode amplitude exceeds a critical value ($A>A_c$). However, for the armchair boundary condition, the mode can exist even when the mode amplitude is above the topological phase transition amplitude and is below a different critical value ($A_c<A<A_c'$). This result can be analyzed by the parameters used in figure 4, where $c_1=1$, $c_2=2$, $c_3=4$, $d_1=4$, $d_2=1.5$, and $d_3=1$. The topological transition amplitude and the critical amplitude are given by $A_c=0.471$ and $A_c'=1.826$, respectively. When we choose the mode amplitude as ($A=0.943$), nonlinear boundary modes cannot exist for the zigzag boundary condition, but nonlinear boundary modes can arise for the armchair boundary condition.

References

[1] Eades J and Hartmann F J 1999 Forty years of antiprotons *Rev. Mod. Phys.* **71** 373–419
[2] Qi X-L and Zhang S-C 2011 Topological insulators and superconductors *Rev. Mod. Phys.* **83** 1057–110
[3] Xiao Di, Chang M-C and Niu Q 2010 Berry phase effects on electronic properties *Rev. Mod. Phys.* **82** 1959–2007
[4] Lubensky T C, Kane C L, Mao X, Souslov A and Sun K 2015 Phonons and elasticity in critically coordinated lattices *Rep. Prog. Phys.* **78** 073901
[5] Kane C L and Lubensky T C 2014 Topological boundary modes in isostatic lattices *Nat. Phys.* **10** 39
[6] Zhou Di, Zhang L and Mao X 2018 Topological edge floppy modes in disordered fiber networks *Phys. Rev. Lett.* **120** 068003
[7] Meeussen A S, Paulose J and Vitelli V 2016 Geared topological metamaterials with tunable mechanical stability *Phys. Rev.* X **6** 041029
[8] Sun K and Mao X 2020 Continuum theory for topological edge soft modes *Phys. Rev. Lett.* **124** 207601
[9] Paulose J, Chen B G and Vitelli V 2015 Topological modes bound to dislocations in mechanical metamaterials *Nat. Phys.* **11** 153–6
[10] Zhou Di, Zhang L and Mao X 2019 Topological boundary floppy modes in quasicrystals *Phys. Rev.* X **9** 021054
[11] Chen Y F, Chen Z G, Ge H, He C, Li X, Lu M H, Sun X C, Yu S Y and Zhang X 2023 Various topological phases and their abnormal effects of topological acoustic metamaterials *Interdiscip. Mater.* **2** 179–230
[12] Chiu C-K, Teo J C Y, Schnyder A P and Ryu S 2016 Classification of topological quantum matter with symmetries *Rev. Mod. Phys.* **88** 035005
[13] Schnyder A P, Ryu S, Furusaki A and Ludwig A W W 2008 Classification of topological insulators and superconductors in three spatial dimensions *Phys. Rev.* B **78** 195125
[14] Hasan M Z and Kane C L 2010 Colloquium: topological insulators *Rev. Mod. Phys.* **82** 3045–67
[15] Su W P, Schrieffer J R and Heeger A J 1979 Solitons in polyacetylene *Phys. Rev. Lett.* **42** 1698–701
[16] Hatsugai Y 1993 Chern number and edge states in the integer quantum Hall effect *Phys. Rev. Lett.* **71** 3697–700
[17] Sone K and Ashida Y 2019 Anomalous topological active matter *Phys. Rev. Lett.* **123** 205502
[18] Hughes T L, Prodan E and Bernevig B A 2011 Inversion-symmetric topological insulators *Phys. Rev.* B **83** 245132
[19] Hatsugai Y 1993 Edge states in the integer quantum Hall effect and the Riemann surface of the Bloch function *Phys. Rev.* B **48** 11851–62
[20] Yang Z, Lustig E, Harari G, Plotnik Y, Lumer Y, Bandres M A and Segev M 2020 Mode-locked topological insulator laser utilizing synthetic dimensions *Phys. Rev.* X **10** 011059
[21] Peláez M, Reinosa U, Serreau J, Tissier M and Wschebor N 2021 Spontaneous chiral symmetry breaking in the massive Landau gauge: realistic running coupling *Phys. Rev.* D **103** 094035
[22] Sheu C-H and Shifman M 2023 Consistency of chiral symmetry breaking in chiral yang-mills theory with adiabatic continuity *Phys. Rev.* D **107** 054030
[23] Rechtsman M C, Zeuner J M, Plotnik Y, Lumer Y, Podolsky D, Dreisow F, Nolte S, Segev M and Szameit A 2013 Photonic floquet topological insulators *Nature* **496** 196–200
[24] Sarma S D, Freedman M and Nayak C 2015 Majorana zero modes and topological quantum computation *npj Quantum Inf.* **1** 1–13
[25] Sone K, Ashida Y and Sagawa T 2020 Topological synchronization of coupled nonlinear oscillators (arXiv:2012.09479)
[26] Zilberberg O, Huang S, Guglielmon J, Wang M, Chen K P, Kraus Y E and Rechtsman M C 2018 Photonic topological boundary pumping as a probe of 4D quantum Hall physics *Nature* **553** 59–62
[27] Noh J, Benalcazar W A, Huang S, Collins M J, Chen K P, Hughes T L and Rechtsman M C 2018 Topological protection of photonic mid-gap defect modes *Nat. Photon.* **12** 408–15
[28] Mukherjee S and Rechtsman M C 2021 Observation of unidirectional solitonlike edge states in nonlinear floquet topological insulators *Phys. Rev.* X **11** 041057
[29] Plotnik Y *et al* 2014 Observation of unconventional edge states in 'photonic graphene' *Nat. Mater.* **13** 57–62
[30] Noh J, Huang S, Leykam D, Chong Y D, Chen K P and Rechtsman M C 2017 Experimental observation of optical Weyl points and Fermi arc-like surface states *Nat. Phys.* **13** 611–7
[31] Lumer Y, Plotnik Y, Rechtsman M C and Segev M 2013 Self-localized states in photonic topological insulators *Phys. Rev. Lett.* **111** 243905
[32] Bekenstein R, Schley R, Mutzafi M, Rotschild C and Segev M 2015 Optical simulations of gravitational effects in the Newton–Schrödinger system *Nat. Phys.* **11** 872–8
[33] Sharabi Y, Sheinfux H H, Sagi Y, Eisenstein G and Segev M 2018 Self-induced diffusion in disordered nonlinear photonic media *Phys. Rev. Lett.* **121** 233901
[34] Lamhot Y, Barak A, Peleg O and Segev M 2010 Self-trapping of optical beams through thermophoresis *Phys. Rev. Lett.* **105** 163906
[35] Ezawa M 2022 Nonlinear non-hermitian higher-order topological laser *Phys. Rev. Res.* **4** 013195
[36] Ezawa M 2023 Nonlinear dynamical topological phases in a cooper-pair box array *Phys. Rev.* B **108** 075412
[37] Isobe T, Yoshida T and Hatsugai Y 2024 Bulk-Edge Correspondence for Nonlinear Eigenvalue Problems *Phys. Rev. Lett.* **132** 126601
[38] Tempelman J R, Matlack K H and Vakakis A F 2021 Topological protection in a strongly nonlinear interface lattice *Phys. Rev.* B **104** 174306
[39] Ablowitz M J and Cole J T 2022 Nonlinear optical waveguide lattices: asymptotic analysis, solitons and topological insulators *Physica* D **440** 133440
[40] Zangeneh-Nejad F and Fleury R 2019 Nonlinear second-order topological insulators *Phys. Rev. Lett.* **123** 053902
[41] Abdullaev F K and Umarov B A 2014 Exact solitonic solutions for optical media with $\chi^{(2)}$ nonlinearity and PT-symmetric potentials *J. Phys.: Conf. Ser.* **553** 012001
[42] Lumer Y, Plotnik Y, Rechtsman M C and Segev M 2013 Nonlinearly induced PT transition in photonic systems *Phys. Rev. Lett.* **111** 263901
[43] Ablowitz M J and Musslimani Z H 2013 Integrable nonlocal nonlinear Schrödinger equation *Phys. Rev. Lett.* **110** 064105
[44] Lu N, Kevrekidis P G and Cuevas-Maraver J 2014 PT -symmetric sine-gordon breathers *J. Phys. A: Math. Theor.* **47** 455101
[45] Ablowitz M J, Been J B and Carr L D 2022 Fractional integrable nonlinear soliton equations *Phys. Rev. Lett.* **128** 184101
[46] Fan Li, Wang J, Varghese L T, Shen H, Niu B, Xuan Y, Weiner A M and Qi M 2012 An all-silicon passive optical diode *Science* **335** 447–50
[47] Schindler J, Li A, Zheng M C, Ellis F M and Kottos T 2011 Experimental study of active LRC circuits with PT symmetries *Phys. Rev.* A **84** 040101

[48] Benisty H *et al* 2011 Implementation of PT symmetric devices using plasmonics: principle and applications *Opt. Express* **19** 18004–19
[49] Ozawa T *et al* 2019 Topological photonics *Rev. Mod. Phys.* **91** 015006
[50] Jezequel L and Delplace P 2022 Nonlinear edge modes from topological one-dimensional lattices *Phys. Rev.* B **105** 035410
[51] Bomantara R W, Zhao W, Zhou L and Gong J 2017 Nonlinear dirac cones *Phys. Rev.* B **96** 121406
[52] Jezequel L, Tauber C and Delplace P 2022 Estimating bulk and edge topological indices in finite open chiral chains *J. Math. Phys.* **63** 12
[53] Sone K, Ezawa M, Ashida Y, Yoshioka N and Sagawa T 2024 Nonlinearity-induced topological phase transition characterized by the nonlinear chern number *Nat. Phys.* (https://doi.org/10.1038/s41567-024-02451-x)
[54] Sone K, Ashida Y and Sagawa T 2022 Topological synchronization of coupled nonlinear oscillators *Phys. Rev. Res.* **4** 023211
[55] Knebel J, Geiger P M and Frey E 2020 Topological phase transition in coupled rock-paper-scissors cycles *Phys. Rev. Lett.* **125** 258301
[56] Umer M and Gong J 2022 Topologically protected dynamics in three-dimensional nonlinear antisymmetric Lotka-Volterra systems *Phys. Rev.* B **106** L241403
[57] Geiger P M, Knebel J and Frey E 2018 Topologically robust zero-sum games and Pfaffian orientation: how network topology determines the long-time dynamics of the antisymmetric Lotka-Volterra equation *Phys. Rev.* E **98** 062316
[58] Mizoguchi T Yoshida T and Hatsugai Y 2021 Chiral edge modes in evolutionary game theory: a kagome network of rock-paper-scissors cycles *Phys. Rev.* E **104** 025003
[59] Yoshida T, Mizoguchi T and Hatsugai Y 2022 Non-Hermitian topology in rock–paper–scissors games *Sci. Rep.* **12** 560
[60] Lo P-W, Santangelo C D, Chen B G, Jian C-M, Roychowdhury K and Lawler M J 2021 Topology in nonlinear mechanical systems *Phys. Rev. Lett.* **127** 076802
[61] Liu K and Paulino G H 2017 Nonlinear mechanics of non-rigid origami: an efficient computational approach *Proc. R. Soc.* A **473** 20170348
[62] Rosa M I N, Pal R K, Arruda J R F and Ruzzene M 2019 Edge states and topological pumping in spatially modulated elastic lattices *Phys. Rev. Lett.* **123** 034301
[63] Ma F, Tang Z, Shi X, Wu Y, Yang J, Zhou Di, Yao Y and Li F 2023 Nonlinear topological mechanics in elliptically geared isostatic metamaterials *Phys. Rev. Lett.* **131** 046101
[64] Hohmann H *et al* 2023 Observation of cnoidal wave localization in nonlinear topolectric circuits *Phys. Rev. Res.* **5** L012041
[65] Wang Y, Lang Li-J, Lee C H, Zhang B and Chong Y D 2019 Topologically enhanced harmonic generation in a nonlinear transmission line metamaterial *Nat. Commun.* **10** 4279
[66] Edgar R S *et al* 2012 Peroxiredoxins are conserved markers of circadian rhythms *Nature* **485** 459–64
[67] Alyatkin S, Sigurdsson H, Askitopoulos A, Töpfer J D and Lagoudakis P G 2021 Quantum fluids of light in all-optical scatterer lattices *Nat. Commun.* **12** 5571
[68] Parker R, Aceves A, Cuevas-Maraver J and Kevrekidis P G 2023 Standing and traveling waves in a model of periodically modulated one-dimensional waveguide arrays *Phys. Rev.* E **108** 024214
[69] Pan Y, Cohen M-I and Segev M 2023 Superluminal k-gap solitons in nonlinear photonic time crystals *Phys. Rev. Lett.* **130** 233801
[70] Vakakis A F, Manevitch L I, Mikhlin Y V, Pilipchuk V N and Zevin A A 2001 *Normal Modes and Localization in Nonlinear Systems* (Springer)
[71] Fruchart M, Hanai R, Littlewood P B and Vitelli V 2021 Non-reciprocal phase transitions *Nature* **592** 363–9
[72] Eckmann J P and Ruelle D 1985 Ergodic theory of chaos and strange attractors *Rev. Mod. Phys.* **57** 617–56
[73] Goel N S, Maitra S C and Montroll E W 1971 On the Volterra and other nonlinear models of interacting populations *Rev. Mod. Phys.* **43** 231–76
[74] Bunin G 2017 Ecological communities with Lotka-Volterra dynamics *Phys. Rev.* E **95** 042414
[75] Brenig L 1988 Complete factorisation and analytic solutions of generalized Lotka-Volterra equations *Phys. Lett.* A **133** 378–82
[76] Vorberg D, Wustmann W, Ketzmerick R and Eckardt A 2013 Generalized bose-einstein condensation into multiple states in driven-dissipative systems *Phys. Rev. Lett.* **111** 240405
[77] Knebel J, Weber M F, Krüger T and Frey E 2015 Evolutionary games of condensates in coupled birth–death processes *Nat. Commun.* **6** 6977
[78] Ma Q, Grushin A G and Burch K S 2021 Topology and geometry under the nonlinear electromagnetic spotlight *Nat. Mater.* **20** 1601–14
[79] Wong S, Loring T A and Cerjan A 2023 Probing topology in nonlinear topological materials using numerical *k*-theory *Phys. Rev.* B **108** 195142
[80] Fronk M D and Leamy M J 2017 Higher-order dispersion, stability and waveform invariance in nonlinear monoatomic and diatomic systems *J. Vib. Acoust.* **139** 051003
[81] See Appendix for the derivation of nonlinear Berry phase, non-spatial symmetries, topological fixed point, and topological phase transitions
[82] Sato M and Ando Y 2017 Topological superconductors: a review *Rep. Prog. Phys.* **80** 076501
[83] Ryu S and Hatsugai Y 2002 Topological origin of zero-energy edge states in particle-hole symmetric systems *Phys. Rev. Lett.* **89** 077002
[84] Iritani R Adachi K and Hamazaki R 2022 universal constraint on nonlinear population dynamics *Commun. Phys.* **5** 129
[85] Ludwig D, Jones D D and Holling C S 1978 Qualitative analysis of insect outbreak systems: the spruce budworm and forest *J. Animal Ecol.* **47** 315–32
[86] Tang J, Ma F, Li F, Guo H and Zhou Di 2023 Strongly nonlinear topological phases of cascaded topoelectrical circuits *Front. Phys.* **18** 33311
[87] Tsapalis A, Politis E P, Maintas X N and Diakonos F K 2016 Gauss' law and nonlinear plane waves for Yang-Mills theory *Phys. Rev.* D **93** 085003
[88] Zhou Di, Zeb Rocklin D, Leamy M and Yao Y 2022 Topological invariant and anomalous edge modes of strongly nonlinear systems *Nat. Commun.* **13** 3379
[89] Chong C, Wang Y, Maréchal D, Charalampidis E G, Molerón M, Martínez A J, Porter M A, Kevrekidis P G and Daraio C 2021 Nonlinear localized modes in two-dimensional hexagonally-packed magnetic lattices *New J. Phys.* **23** 043008
[90] Chen Y-A, Huber S D, Trotzky S, Bloch I and Altman E 2011 Many-body Landau–Zener dynamics in coupled one-dimensional Bose liquids *Nat. Phys.* **7** 61–67

[91] Tuloup T, Bomantara R W, Lee C H and Gong J 2020 Nonlinearity induced topological physics in momentum space and real space *Phys. Rev.* B **102** 115411
[92] Koller S B, Goldschmidt E A, Brown R C, Wyllie R, Wilson R M and Porto J V 2016 Nonlinear looped band structure of Bose-Einstein condensates in an optical lattice *Phys. Rev.* A **94** 063634
[93] Liu J, Wu B and Niu Q 2003 Nonlinear evolution of quantum states in the adiabatic regime *Phys. Rev. Lett.* **90** 170404
[94] Pu H, Maenner P, Zhang W and Ling H Y 2007 Adiabatic condition for nonlinear systems *Phys. Rev. Lett.* **98** 050406
[95] Liu J and Fu L B 2010 Berry phase in nonlinear systems *Phys. Rev.* A **81** 052112
[96] Litvinets F N, Shapovalov A V and Trifonov A Y 2006 Berry phases for the nonlocal gross–pitaevskii equation with a quadratic potential *J. Phys. A: Math. Gen.* **39** 1191
[97] Abeya A, Biondini G and Hoefer M A 2023 Whitham modulation theory for the defocusing nonlinear Schrödinger equation in two and three spatial dimensions *J. Phys. A: Math. Theor.* **56** 025701
[98] Minzoni A A and Smyth N F 2016 Modulation theory, dispersive shock waves and gerald beresford whitham *Physica* D **333** 6–10
[99] Biondini G, Chong C and Kevrekidis P 2023 On the whitham modulation equations for the toda lattice and the quantitative characterization of its dispersive shocks (arXiv:2312.10755)
[100] Konotop V V, Yang J and Zezyulin D A 2016 Nonlinear waves in $\mathcal{PT}$-symmetric systems *Rev. Mod. Phys.* **88** 035002
[101] Christodoulides D *et al* 2018 *Parity-Time Symmetry and its Applications* vol 280 (Springer)
[102] Haim A and Oreg Y 2019 Time-reversal-invariant topological superconductivity in one and two dimensions *Phys. Rep.* **825** 48
[103] Ryu S, Schnyder A P, Furusaki A and Ludwig A W W 2010 Topological insulators and superconductors: tenfold way and dimensional hierarchy *New J. Phys.* **12** 065010
[104] Dumitrescu E, Sau J D and Tewari S 2014 Magnetic field response and chiral symmetry of time-reversal-invariant topological superconductors *Phys. Rev.* B **90** 245438
[105] Zhou Di and Zhang J 2020 Non-hermitian topological metamaterials with odd elasticity *Phys. Rev. Res.* **2** 023173
[106] Sticlet D 2012 Edge states in chern insulators and majorana fermions in topological superconductors
[107] Li C and Kartashov Y V 2023 Topological gap solitons in Rabi Su-Schrieffer-Heeger lattices *Phys. Rev.* B **108** 184301
[108] Strogatz S H 2018 *Nonlinear Dynamics and Chaos with Student Solutions Manual: With Applications to Physics, Biology, Chemistry and Engineering* (CRC Press)
[109] Wang A, Zhou Y and Chen C Q 2023 Topological mechanics beyond wave dynamics *J. Mech. Phys. Solids* **173** 105197
[110] Zhou Y, Zhang Y and Chen C Q 2021 Amplitude-dependent boundary modes in topological mechanical lattices *J. Mech. Phys. Solids* **153** 104482
[111] Zhou Y, Zhang T, Long J, Wang A and Chen C Q 2024 Static vector solitons in a topological mechanical lattice *Commun. Phys.* **7** 131
[112] Wang A, Meng Z and Chen C Q 2023 Non-Hermitian topology in static mechanical metamaterials *Sci. Adv.* **9** eadf7299
[113] Guo X, Jezequel L, Padlewski M, Lissek H, Delplace P and Fleury R 2024 Practical realization of chiral nonlinearity for strong topological protection (arXiv:2403.10590)